Reactive RF Sputtering of VO_2

by

Grigory Chugunov

A thesis
presented to the University of Waterloo
in fulfilment of the
thesis requirement for the degree of
Master of Applied Science
in
Electrical and Computer Engineering

Waterloo, Ontario, Canada, 2016
© Grigory Chugunov 2016

Author's Declaration

I hereby declare that I am the sole author of this thesis. This is a true copy of the thesis, including any required final revisions, as accepted by my examiners.

I understand that my thesis may be made electronically available to the public.

Abstract

There are multiple oxides that exhibit metal-to-insulator transition, VO_2 is one of them. What makes it unique is that the transition occurs at near room temperature, thereby making the energy cost of switching very low. The material had amassed a large amount of attention from scientific community over the past few years, resulting in low power devices like phase change field-effect transistors with switching times on the order of picoseconds. The deposition of VO_2 can be approached via chemical vapour deposition, evaporation, sputtering, or sol-gel. The focus of my work was the reactive RF sputtering approach to depositing polycrystalline VO_2 thin films. The optimal deposition parameters were demonstrated to be 500℃ substrate temperature and 10.2%-10.3% partial oxygen flow using a 2" target at 200W RF power. Resulting growth rate was about 1.5 nm/min. The quality of VO_2 was studied using device level S-parameter measurements of insertion loss using vector network analyzer while changing temperature from 25℃ to 100℃. Future plans for further improvement of the material deposited and solutions for localized heating using wave-shaped Au/Cr micro-heaters are provided.

Acknowledgements

I would like to extend a heartfelt thank you to Professor Raafat Mansour for his bottomless patience and endless support throughout my research career. None of this would be possible without him.

I also want to express my gratitude to Professor Guo-Xing Miao for his assistance with XRD measurements and valuable advices concerning VO_2.

It would be unfair for me to not mention Frank Jiang, a fellow graduate student who readily offered his help countless times while being buried under a mountain of work himself.

I would not be able to get over my writer's block without honest and constructive criticism from Professor Chris Backhouse.

I would like to thank Saman Nazari and Olzhas Tazabekov for always being ready to bounce ideas with a cup of coffee in hand.

The experimental part of my work would be impossible without Bill Jolley and Nathan Nelson-Fitzpatrick and their dedication to their clean rooms.

Last, but not least, I would like to bow to the entire CIRFE community for being there for me.

Dedication

This thesis is dedicated to my parents and to my better half for forcing me to move forward, even when it was difficult.

Contents

Author's Declaration ii
Abstract iii
Acknowledgements iv
Dedication v
List of Figures vii
List of Tables ix
List of Abbreviations x

1 Introduction **1**

2 Literature Review **3**
2.1 Theory 4
2.2 Deposition 6
2.2.1 CVD 6
2.2.2 Evaporation 8
2.2.3 Sputtering 10
2.2.4 Wet-coating & Doping 11
2.3 Applications 13
2.3.1 Localized Heating 14

3 Methodology And Results **17**
3.1 Collaboration 17
3.2 Equipment 18
3.3 Initial Work 20
3.4 Parametrics 24
3.4.1 Partial Oxygen Flow Parametric Study 25
3.4.2 Deposition Rate and Temperature Studies 31
3.5 Heating 33

4 Discussion **36**
4.1 Conclusion 39

A Micro-heating **41**

Bibliography **52**

List of Figures

2.1 Schematic of an electric-double-layer transistor (EDLT) based on VO_2, potentially enabling electrical switching of the MIT between the metallic tetragonal phase and the insulating monoclinic phase [4]. 7
2.2 Tetragonal unit cell of the high-temperature phase of vanadium dioxide [9]. 7
2.3 Temperature dependence of the resistivity of strained 10-nm and relaxed 70-nm VO_2 films grown on TiO_2 substrate [4]. 7
2.4 Schematic energy diagrams of the 3d bands around the Fermi level for VO_2 [10]. 7
2.5 Monoclinic structure of the low-temperature phase of VO_2 and its relationship to the rutile structure [9]. 7
2.6 AFM images of the VO_2 films: (a) a 270-nm-thick film deposited on bare Si at 500℃, (b) a 260-nm-thick film deposited on bare Si at 400℃, (c) a 350-nm-thick film deposited on V nucleated Si at 300℃, with the inset showing a 250x250 nm surface of the 10-nm-thick V underlayer deposited on Si [23]. 12
2.7 Deposition rate as a function of oxygen flow ratio and substrate temperature [23]. 12
2.8 Major phases identified by XRD in the films deposited on Si under various conditions of substrate temperature and oxygen flow ratio [23]. 12
2.9 Top view of layers of the VO_2 thin-film switch with a cross-sectional view showing the Pt heating coil on the top layer, then SiO_2, Au, VO_2, and sapphire substrate [37]. 16
2.10 S_{11} and S_{21} of measured results and S_{11} and S_{21} of electrical model matched results at 20℃ [37]. 16
2.11 S_{11} and S_{21} of measured results and S_{11} and S_{21} of electrical model matched results at 80℃ [37]. 16
2.12 Temperature profile of wave-shaped heater from experiment [44]. . . 16
2.13 Temperature distribution in the wave-shaped heater from (Figure 2.12) [44]. 16
2.14 COMSOL simulation results for a spiral-shaped heater [43]. 16

3.1 Equipment 21
3.2 XRD patterns of VO_x films at various oxygen flow ratios. (a) 7.5% (b) 10% (c) 12.5% 23

3.3 Sample SIMS data for VO_x etching process using ionmill. (a) Power setting 1 (b) Power setting 2 25
3.4 Masks used for (a) Au patterning and (b) VO_x patterning 26
3.5 General process for device microfabrication used in this project 28
3.6 S_{21} analysis of partial oxygen flow studies. "hot" refers to 100°C+ and "cold" refers to room temperature. (a)11%-10.25% (b)10.20%-9.8% (c)10.3%-9.4%, much thicker films 29
3.7 Fabricated devices included in the mask layout for this project. The number above the device defines the size of the gap or the width of the short in um. (a) DC switches with variable gaps (b) CPW series switches ver1, with variable gaps (c) CPW parallel switches ver1, with variable shorts (d) CPW series switches ver2, with variable gaps (e) CPW parallel switches ver2, with variable shorts. 30
3.8 Deposition rate behaviour with (a) change in partial oxygen flow and (b) time 31
3.9 S_{21} analysis of samples deposited at variable substrate temperatures . 33
3.10 Custom design of a wave-shaped micro-heater 35

List of Tables

3.1 VO_x chart in accordance to partial oxygen flows during deposition . . 22
3.2 Ionmill etching rates for VO_x 24
3.3 Power and voltage response to oxygen flow change, at the target of the sputtering system 32
3.4 Dependence of deposition rate of VO_x on substrate temperature . . . 32

List of Abbreviations

ARE activated reactive evaporation. 8, 9

CIRFE Centre for Integrated RF Engineering. 2, 19, 36, 39

CPW coplanar waveguide. 24, 26, 32

CVD chemical vapour deposition. 6, 8, 10, 13

DC direct current. 10

EACVD electric field assisted ACVD. 6, 8

EDLT electric-double-layer transistor. vii, 7

MEMS microelectromechanical systems. 13, 14, 38

MIT metal-to-insulator transition. 1, 3–6, 11, 24, 38

MOCVD metal-organic CVD. 6, 8

PLD pulsed laser deposition. 8–10

PR photoresist. 10, 19, 22, 24

RF radio frequency. 1, 2, 10, 11, 13, 17, 20

SEM scanning electron microscopy. 39

SIMS secondary ion mass spectroscopy. 22

UHV ultra high vacuum. 11

VNA vector network analyzer. 20, 26, 32

XRD x-ray diffraction. 1, 20, 22, 39

Chapter 1

Introduction

The fast-paced world we live in constantly demands higher speeds and lower power consumption from mobile electronics, even while industry is searching for simplicity of design. According to the latest research, VO_2 is a viable solution. In general terms, VO_2 is a phase change material that exhibits metal-to-insulator transition (MIT)[1] at near room temperature. The resulting increase in conductivity is by a factor of 10^5, thus giving VO_2 metallic-like properties. The transition speed is on the order of nanoseconds to picoseconds, depending on the activation method.

The focus of my work is development of a deposition method for polycrystalline VO_2 thin films. Prior to the commencement of my study, no such method was yet available on the campus of the University of Waterloo. The early stage of my research involved reviewing the literature for already established deposition procedures as well as collaborating with external research groups in the field. Once I accumulated enough knowledge on the subject, I located the deposition equipment needed on site. I then gained the training required to operate the equipment and procured all the materials needed. Initially, x-ray diffraction (XRD) measurements were used to characterize the thin films deposited. Once samples exhibiting MIT were obtained, I designed 2-port radio frequency (RF) switches based on the phase change material. The insertion loss[2]of the devices was measured in several parametric studies to further improve the

[1] A transition from metal-like high conductivity state to the one of insulator. In context of this work, the transition is activated by a change in temperature of the material.

deposition recipe of VO_2. The ultimate goal is to obtain series RF switches with over 30 dB port isolation and less than 1 dB insertion loss when in the ON state.

A detailed literature review is provided in Chapter 2. It focuses on the deposition methods of VO_2, introduces the theoretical background, and highlights some of applications of the material. Chapter 3 is dedicated to methodology and results and demonstrates my reactive RF sputtering approach to VO_2 deposition. It also shows the work that was done to further improve the recipe. The final chapter discusses, summarizes and concludes my findings.

This project demonstrates a unique method to VO_2 quality characterization. It also shows how and why the material fits perfectly with the RF microfabrication process already established at the Centre for Integrated RF Engineering (CIRFE) at the University of Waterloo. That said, the recipe presented is still in the development phase, with future steps for its improvement discussed in Chapter 4.

[2]A loss of signal power resulting from insertion of the device. Considering series RF switches used in my research, it is expected to have high insertion loss at low temperature, when VO_2 is insulative, and low insertion loss at high temperature, when VO_2 is conductive.

Chapter 2

Literature Review

F. J. Morin is a name closely associated with VO_2. Morin was the first to bring VO_2 to the attention of the scientific community back in 1959 as one of "oxides which show a metal-to-insulator transition at the neel temperature" [1]. Even in the world of materials that exhibit MIT, VO_2 stands out. The activation of the phase transition in the oxide was demonstrated via numerous methods, including thermal [2], optical [3], electrical field induced [4], mechanical [5], voltage pulses [6] and charge injection [7]. The property change of the material which accompanies the phase transition is not limited to resistivity but includes transmittance, dielectric constant and other factors [2]. From a thermal perspective, the transition occurs at near room temperature. In cases of bulk and relaxed thin films, it takes place at around 68℃ [2]. Additionaly, a new type of field-effect[1] device based on VO_2 was recently unveiled by M. Nakano et al. [4] with switching speeds on the order of picoseconds. From this, we can see that VO_2, high speed and low power consumption go hand-in-hand.

The literature review presented in this chapter starts with a theoretical introduction to MIT in VO_2, followed by an extended coverage of deposition methods in section 2.2. The final section brings to light some of applications of the material. A basic understanding of microfabrication and physics are expected, footnotes with some additional insights are provided.

[1]The MIT is triggered by an electric field.

2.1 Theory

As was previously stated, F. J. Morin [1] is responsible for some of the earliest theoretical and experimental work in the field of lower oxides[2] that undergo MIT. In his studies, Morin explored titanium and vanadium oxides, including VO_2. One of Morin's suggestions was that t_2g orbitals of 3d[3] series oxides extend into a narrow conduction band, thus leading to metallic behaviour. He did admit that the case of VO_2 seems to be more complex than that of titanium oxides, since t_2g orbitals were found to be partially empty in the low temperature phase and thus fail to support the insulating behaviour of the material. These observations led to his conclusion that there are two competing processes. The first is the correlation effect that tends to localize the d electrons, thus promoting insulator behaviour. The second process is the tendency of electrons to delocalize by spreading into bands, thereby promoting metallic behaviour. Morin claimed that the transition in all of the oxides can be described by a partially filled conduction band which splits into an empty upper band and a filled lower band. Here, all of the levels are localized and have an antiferromagnetic spin alignment. In my opinion, Morin's work is one of cornerstones of VO_2 research.

Nearly a decade later, theoretical work in VO_2 was picked up by John B. Goodenough [8], who attempted to build a connection between the structural transition of VO_2 and band theory. It is important to mention that the growth of VO_2 had greatly improved by this time, with some experimental results showing a 5 orders of magnitude change in resistivity, whereas with F. J. Morin [1] it was only 2 orders. Such a drastic experimental change required a better theoretical explanation. Structure-wise, high temperature VO_2 is a rutile tetragonal (Figure 2.2) which shifts to monoclinc (Figure 2.5) during the transition. A feature of note is that the shift results in the formation of V-V pairs, which are not present at high temperature. The resulting structure also possesses the shortest V-O bonds, one per V-V pair. This feature suggests that an antiferroelectric distortion coincides with the transition of VO_2 to an

[2]The oxide's stoichiometry can be described by $X_nO_{m\leq 2n}$ formula

[3]d orbitals can be split into two energy levels. The higher energy level is referred as t_2g, triply degenerate orbitals with even shape.

insulative state. One of his main arguments was that the driving mechanism for the MIT in VO_2 is the antiferroelectric transition.

A few years later, a counterargument to the above approach was presented by A. Zylbersztejn and N. F. Mott [9]. It was stated that the band theory is insufficient at above zero temperature. A conductivity jump of 5 orders can only be explained by an increase either in carrier count or carrier mobility. The structural shift on its own is not enough to produce a gap required for such a transition. It was also stated that in order to give a quantitative description, Hubbard intra-atomic correlation energy[4] needs to be taken into account, since the formed gap is mainly a consequence of single-electron centers forming pairs. Keep in mind that the transition cannot be explained simply by the Mott-Hubbard model. Even though the upper Hubbard band is empty and separated from the lower, the broad π^*[5] band is not split and lies above the lower edge, and so the Hubbard gap is located between the lowest half of the split $d_{||}$ band and the π^* band (Figure 2.4). It was concluded that the pairing of the V ions in VO_2 has only a minor effect on the formed gap, and that for further understanding electron-electron interactions need to be accounted for.

The above two works led to somewhat of a stalemate in VO_2 transition theory, after which the works were reexamined by D. Paquet and P. Leroux-Hugon [11]. Paquet and Leroux-Hugon had unified a number of accepted theoretical schemes, which were put forward in prior literature, in an attempt to reach a consensus. Instead of focusing on electron-electron interactions and structural interactions separately, the researchers combined the two. The reason behind this approach is that the correlation gap in the $d_{||}$ appears to be smaller in the presence of the structural distortion. Paquet and Leroux-Hugon also found that a multiband approach to the model resulted in a first-order transition with a rather high transition temperature, while focusing solely on $d_{||}$ electron interactions resulted in a second-order transition at a lower temperature.

In summary, VO_2 thermoelectric phase change is considered to be a first-order

[4]Hubbard energy model consists out of two terms, a kinetic term to describe tunneling and a potential term to describe on-site lattice interactions.

[5]Triply degenerate t_2g levels are further split into the π^* and $d_{||}$ levels by the orthorhombic component of the tetragonal crystal field [10].

MIT driven by electron-electron localization and delocalization, which is supported by the structural shift of the oxide from tetragonal to monoclinic. In its high temperature, tetragonal state all V atoms are isolated and do not directly interact. During monoclinic distortion, V^{4+} atoms are brought closer together, thus creating a localized electron-pair trap. From the band perspective, this can be visualized as a combined, half-filled band formed by π^* and $d_{||}$ orbitals at high temperature. When material is cooled down to below transition temperature, $d_{||}$ splits, upper half and π^* shift to higher state, thus forming a gap between the full bottom half of $d_{||}$ and empty π^*.

2.2 Deposition

Over the years, numerous methods of VO_2 deposition were proposed and implemented, ranging from chemical vapour deposition (CVD) [12]–[14] to evaporation [15]–[22], sputtering [23]–[27] and more [28], [29]. The choice of the method comes down to required deposition rates, substrate size/type, maximum and minimum film thicknesses, and acceptable process temperature. There are many parameters to consider prior to making the choice, if such a choice exists.

2.2.1 CVD

In the past, multiple processes were successfully applied for CVD of VO_2, including metal-organic CVD (MOCVD) [12], electric field assisted ACVD (EACVD) [13], and pyrolysis [14]. The main differences between the three approaches are deposition rates and microstructures of resulting films.

H. K. Kim et al. [12] demonstrated epitaxially grown VO_2 films using MOCVD. The process exhibits low deposition rates (thickness of films deposited ranges from 60 to 310 Å), and the resulting films are very smooth. Due to the epitaxial nature of the process, a choice of substrate/buffer layer with similar 2D crystallography to VO_2 is necessary. In this specific case, TiO_2 was used as the buffer layer due to its compatibility with sapphire substrate as well as VO_2. The oxide phase of vanadium is controlled by the flow rate of the oxidant, O_2, as well as deposition temperature,

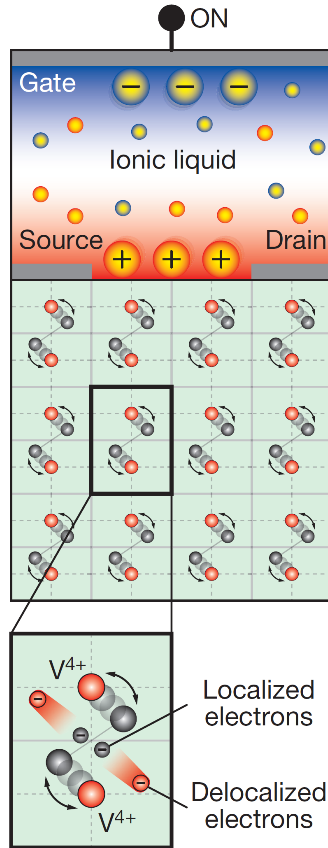

Figure 2.1: Schematic of an EDLT based on VO_2, potentially enabling electrical switching of the MIT between the metallic tetragonal phase and the insulating monoclinic phase [4].

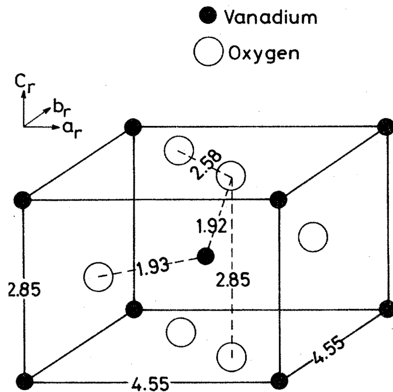

Figure 2.2: Tetragonal unit cell of the high-temperature phase of vanadium dioxide [9].

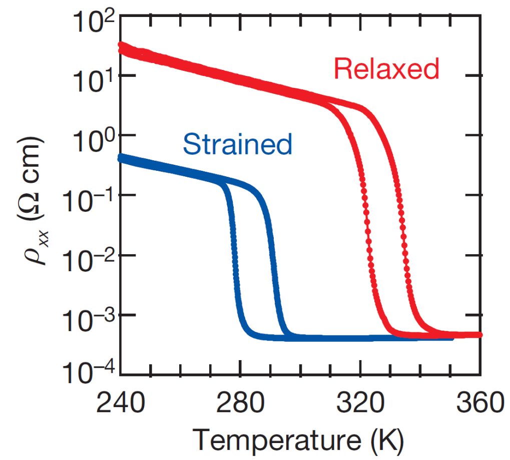

Figure 2.3: Temperature dependence of the resistivity of strained 10-nm and relaxed 70-nm VO_2 films grown on TiO_2 substrate [4].

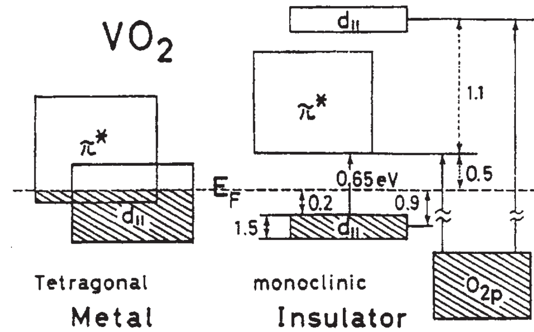

Figure 2.4: Schematic energy diagrams of the 3d bands around the Fermi level for VO_2 [10].

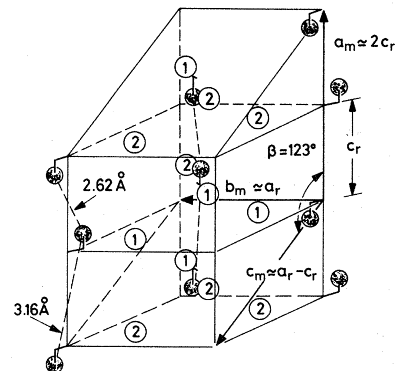

Figure 2.5: Monoclinic structure of the low-temperature phase of VO_2 and its relationship to the rutile structure [9].

500℃. Please refer to [12] for a more detailed description of the recipe as well as the deposition setup.

An EACVD study of VO_2 was performed by Michael E.A. Warwick et al. [13]. This process allows for higher deposition rates (sample thicknesses are 100-2000 nm) with relatively high film roughness. Vanadium oxide control is achieved via oxidant, O_2, flow rate, and deposition temperature, 530℃. The strength of the applied electric field is directly related to the deposition rate and surface microstructure/roughness of the film. Higher strength leads to thicker films with topography that is more porous and rough. The author reported no significant change in thermochromic performance of the films due to the field strength.

The pyrolysis of various vanadium oxide films was demonstrated by L. A. Ryabova et al. [14]. Control over the oxide phase is mainly done via the oxidant, O_2, flow rate. It is difficult to judge the deposition rate from the information provided, but in my opinion it should be comparable to EACVD. The publication stated that the deposited films were very smooth, with grain sizes of about 100 nm in diameter. The deposition temperature is dictated by the material that is being thermally decomposed.

Depending on the application, one CVD method might be preferred over the others. EACVD and pyrolysis are more suitable for thicker films. Also, EACVD is capable of producing highly porous films, which might be of interest for sensing applications [13]. On the other hand, MOCVD can be used to grow highly crystalline films with very precise thickness.

2.2.2 Evaporation

The evaporation approach to deposition of VO_2 films can be traced back to the early 1980s and has since gone through many modifications. Earlier methods involved e-beam evaporation of pure vanadium at ambient temperatures, followed by lengthy annealing. The process was further modified by the introduction of ion assisted deposition [15], [16], background gas [16], heated substrate [17] and activated reactive evaporation (ARE) [20]. Replacement of e-beam evaporation with pulsed laser deposition (PLD) [21], [22] further promoted results in the field.

Advancements in the e-beam evaporation of VO_2 can be seen in research by F. C. Case [15]–[20]. In his earlier works, Case oxidized 3000Å e-beam evaporated vanadium films in oxygen at high temperatures of 400℃-600℃. Depositions were performed on various substrates, which demonstrated that the main reason for incompatibility is a miss-match in thermal expansion coefficients. Such a miss-match can lead to strain build-up within the thin film and thus affecting its performance (Figure 2.3). Case also incorporated low energy ion bombardment into the process. The results of this implementation are somewhat similar to doping of VO_2 (to be reviewed later) or to the strain mentioned previously. There is a distinct shift in transition temperature as well as in optical and electrical properties of both phases. Interestingly, the transition ratio was somewhat constant, unlike in instances where VO_2 is doped or strained.

In his latter works, Case introduced substrate temperature of 400℃+ as well as O_2 as a background gas, which allowed for the forfeiting of the annealing step of the process. A study of note is his publication [17] on the topic of low temperature VO_2 evaporation, where he subsidized some of the substrate temperature with ion bombardment, thus allowing for deposition at 300℃. In the mid-1990s, Case introduced the concept of ARE, in which he placed an anode half-way between the melt and the substrate, thereby promoting the ionization of the background gas. This approach led to VO_2 films with sharper transition and higher contrast. I consider his work a must-read for anyone in the VO_2 evaporation research field.

As stated by D. H. Kim et al. [22], higher operational background pressure is the main benefit of a PLD system. This is especially beneficial when it comes to deposition of oxide thin films. In this specific case, a V_2O_3 target was used, but a pure vanadium target can be utilized as well, as demonstrated by M. Borek et al. [21]. The control over the oxide phase is achieved by adjusting the Ar to O_2 ratio in the chamber as well as the deposition temperature. No postannealing is required. The deposition rate is very high, thus allowing for films that are microns thick.

In my opinion, one of the best features of evaporation techniques is poor step-coverage, which allows for a lift-off approach to patterning. Unfortunately, high deposition temperatures makes the VO_2 process incompatible with most common

photoresists (PRs), hence the attempts to lower the deposition temperature. A lower temperature would allow for more freedom in the general fabrication process. Overall, I find the quality of PLD and e-beam evaporated films comparable. The main difference between the two systems is that PLD generally accepts much smaller substrate sizes than CVD but has a higher deposition rate.

2.2.3 Sputtering

There are a few examples of direct current (DC) [27] sputtering of VO_2, but due to the problem with target poisoning[6], RF sputtering is much more common. RF sputtering also allows for the use of targets other than pure vanadium, such as V_2O_3 and V_2O_5 [24]. The main challenge, as in other deposition approaches, lies in temperature and oxidant control [23], [25].

Ping Jin et al. [23] performed a highly detailed study of reactive RF sputtering of VO_2 at different O_2 flow ratios (0%-8%) and temperatures (250℃-500℃), Figure 2.8. Overall, higher temperatures result in rougher but more crystalline VO_2 with better switching capabilities (Figure 2.6). The acceptable O_2 flow ratio range is greater at higher temperatures, thus making single-phase VO_2 deposition somewhat easier. Deposition rates seem to be independent from the substrate temperature (Figure 2.7). Nevertheless, single-phase VO_2 can be achieved at a temperature as low as 250 ℃ by incorporating very precise oxygen control, vanadium nucleation of the substrate, and negative substrate bias.

When a pure vanadium target is used, the VO_2 deposition occurs in the so-called transition region where the deposition rate changes drastically with the smallest shift in O_2 flow [23] (Figure 2.7). According to Yuzo Shhingesato et al. [24], this can be avoided by introducing alternative targets, such as V_2O_3 and V_2O_5. In the case of V_2O_5, hydrogen is used as the background gas to reduce the resulting thin film. In conclusion, films were found to exhibit wider distribution of transition temperatures, which implies inhomogeneity and strain within the microstructure.

[6] Reactive DC sputtering may lead to oxidation of the target's surface, thus impeding the sputtering process or even stopping it completely.

Overall, sputtering is a good approach for large-area uniform deposition of VO_2. Deposition rates are mainly dependent on the type and size of the target. There are several examples of epitaxially grown VO_2 using ultra high vacuum (UHV) RF sputtering systems [24], [26], thus making it a very flexible method of deposition for various applications of the oxide.

2.2.4 Wet-coating & Doping

As the final step of this section, I would like to mention wet-coating approaches to depositing VO_2, such as sol-gel [28] and aqueous solution [29]. I would also like to introduce doping, which is one of the main methods for manipulating transition temperatures and curves of the films.

Wet-coating methods can be very crudely generalized as the deposition of a vanadium-based film via either dip or spin coating followed by prolonged annealing. The resulting films tend to exhibit a very wide hysteresis, with lower contrast and less sharp transition in comparison to other deposition methods. Considering that these films originate from a liquid phase, they are also quite rough and have occasional micro-gaps. On the other hand, the size of the substrate is theoretically unlimited, which can be of a great benefit for VO_2 applications such as so-called Smart Windows [30]. Working with a liquid phase also provides an easy way of adding dopants.

As mentioned previously, VO_2 MIT occurs at 68℃. This temperature, along with the transition curve, can be altered by the introduction of the dopants W, Ti, Mg, Nb, Cr, Al and Mo [31]–[36]. It is important to mention that thermochromic effects due to dopants do not always coincide with thermoelectric effects. VO_2 doped with W will have a less resistive insulating phase and a lower transition temperature, while Ti doping will lead to a higher resistive metal phase and a higher transition temperature. In both cases, however, the transition contrast and sharpness are somewhat forfeited when film is doped. From a thermochromic perspective, the transition temperature shift is the same, but both phases are affected. For example, in the case of Ti, while the insulating phase becomes less transparent, the metal phase becomes more transparent.

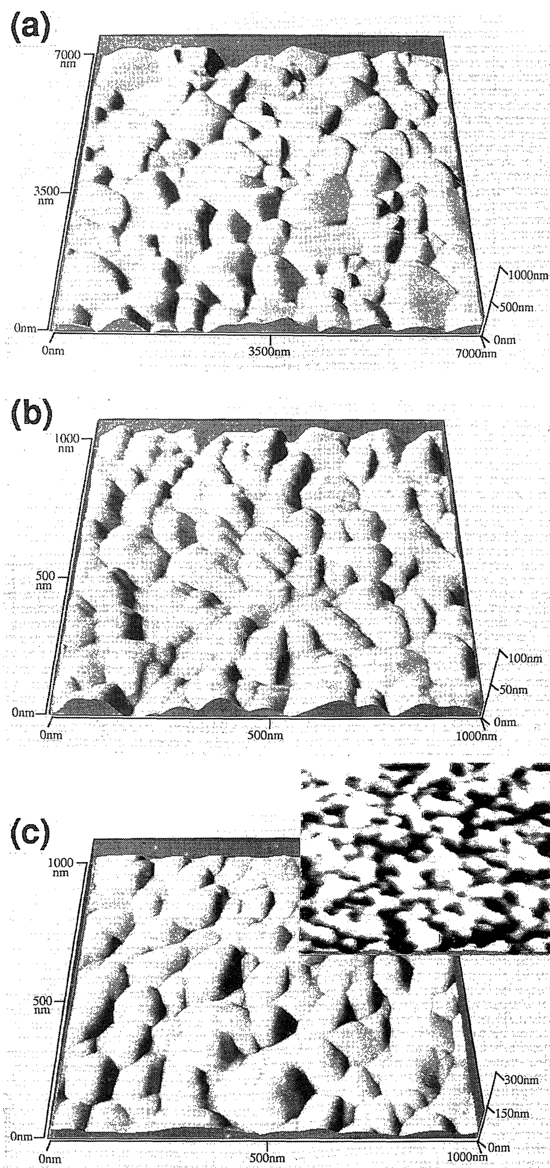

Figure 2.6: AFM images of the VO_2 films: (a) a 270-nm-thick film deposited on bare Si at 500℃, (b) a 260-nm-thick film deposited on bare Si at 400℃, (c) a 350-nm-thick film deposited on V nucleated Si at 300℃, with the inset showing a 250x250 nm surface of the 10-nm-thick V underlayer deposited on Si [23].

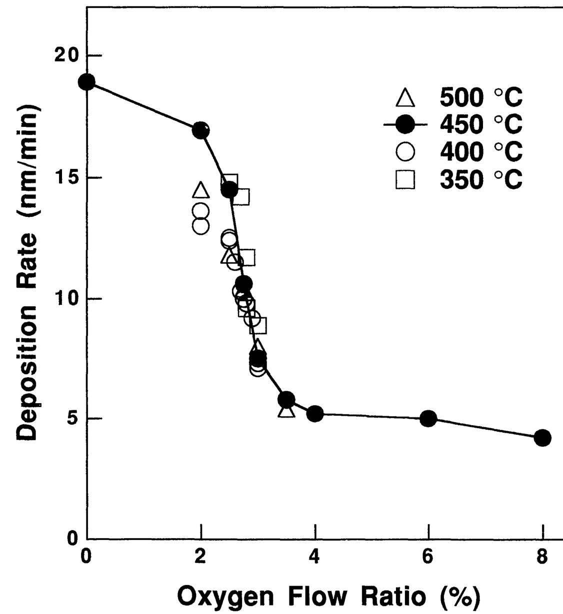

Figure 2.7: Deposition rate as a function of oxygen flow ratio and substrate temperature [23].

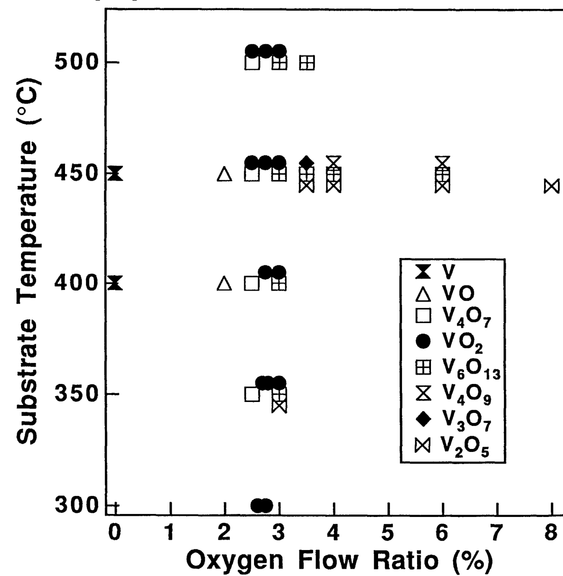

Figure 2.8: Major phases identified by XRD in the films deposited on Si under various conditions of substrate temperature and oxygen flow ratio [23].

Doping VO_2 is not limited to wet coating, from a process and equipment perspectives it is easier. Doping can also be accomplished using CVD, evaporation and sputtering methods. This is achieved by altering the gas mixture, introducing an ion beam for dopant implantation and co-sputtering from multiple targets.

2.3 Applications

Reviewing VO_2 applications is a tremendous task on its own, given the multitude of ways that phase change can be induced in the oxide and the resulting effects on properties such as conductivity, transmittance and dielectric constant, making what can be done with the material somewhat limitless. In this section, I will highlight some examples of VO_2-based switches [37]–[39] as well as the concept of the Smart Window [40], [41].

In a recent work, KuanChang Pan et al. [37] demonstrated the use of VO_2 for a thin film varistor (Figure 2.9). They designed and fabricated series-single-pole single-throw switches, that demonstrated an insertion loss of less than 3 dB (Figure 2.11) and an isolation of more than 30 dB (Figure 2.10). Granted, these results might not be as impressive as some microelectromechanical systems (MEMS) RF switches [42], but the simplicity of their design and short switching time are also advantageous when it comes to reconfigurable electronics. A different research group demonstrated that VO_2-based RF switches can claim high stability to cycling, even without any special packaging [38]. This was found to be especially true if the switch is current-driven instead of voltage-driven.

A different take on VO_2-based switch design was presented by Arash Joushaghani et al. [39] at the University of Toronto. They designed and fabricated a sub-volt broadband hybrid plasmonic switches. The devices were found to operate at near 1550 nm wavelength with a bandwidth of 100 nm. The power consumption was found to be relatively low, 400 mV provided an extinction ratio of more than 20 dB. Such a performance level already makes the device comparable to dielectric counterparts, but the authors believe that it is not the limit. They suggest that by inducing phase

transition in VO_2 via an electric field a new level of ultra-high-speed and low-power modulation can be achieved.

An alternative application for VO_2 involves Smart Windows [40]. The concept of the thermochromic window is an old one, and it likely originated with the discovery of VO_2. The general idea is to adjust the transmittance of the window based on the temperature indoors or outdoors, or a combination of the two. An obvious advantage would be energy savings through passive temperature control. Pure VO_2 does have some shortcomings in this application, which can be summarised as low visible light transmission, unattractive visible colors, and a limited solar spectrum regulating ratio. Nevertheless, all these issues create new topics for research and are currently being addressed [41]. One solution that was mentioned previously is the introduction of dopants.

2.3.1 Localized Heating

When it comes to thermally operated electronic micro-devices, one issue that arises is temperature control. VO_2 phase transition can be induced in many ways, which might explain why this particular topic of activation is not very active. Nonetheless, I do believe that it has some merit. As mentioned previously, thermal phase transition in the material can be induced at relatively low temperatures, thus making the micro-heating task somewhat similar to that of MEMS sensors. This is currently an active field of research, so there are plenty of opportunities for a cross-over.

The two most common approaches are spiral-shaped [43], (Figure 2.14) and wave-shaped [44] (Figure 2.12 and Figure 2.13) designs. A spiral-shaped design provides better control over the "hot spot", whereas a wave-shaped design is more flexible in terms of aspect ratio. The performance and power consumption are largely dependent on the material choice. Susmita et al. [43] demonstrated the use of novel nickel alloy, which has very low input power consumption. Additionally, K. L. Zhang et al. [44]demonstrated that there is room for simplicity when it comes to fabrication. Their example of micro-heaters utilized Ti as the resistive material and Au as the conductor for contacts.

Overall, I think that this is something to be considered. Maybe not for high speed electronics, but as I have previously stated, that is not the only application.

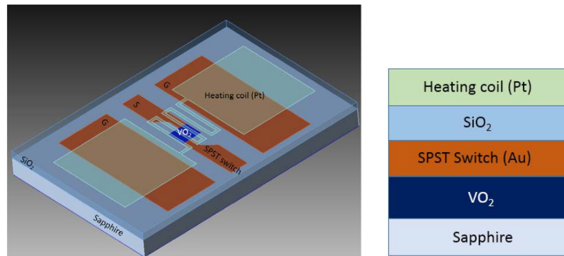

Figure 2.9: Top view of layers of the VO_2 thin-film switch with a cross-sectional view showing the Pt heating coil on the top layer, then SiO_2, Au, VO_2, and sapphire substrate [37].

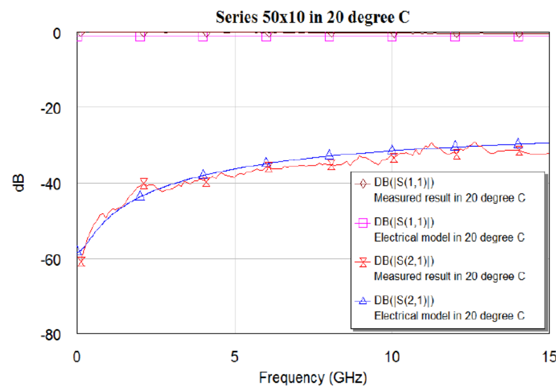

Figure 2.10: S_{11} and S_{21} of measured results and S_{11} and S_{21} of electrical model matched results at 20°C [37].

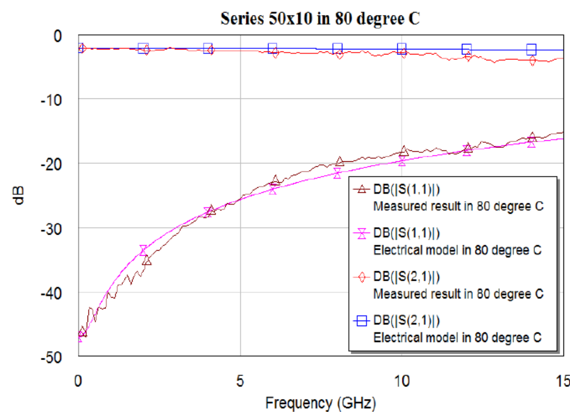

Figure 2.11: S_{11} and S_{21} of measured results and S_{11} and S_{21} of electrical model matched results at 80°C [37].

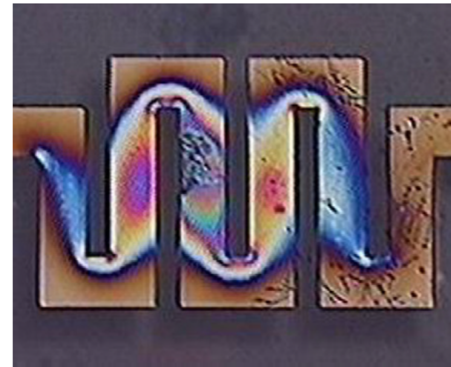

Figure 2.12: Temperature profile of wave-shaped heater from experiment [44].

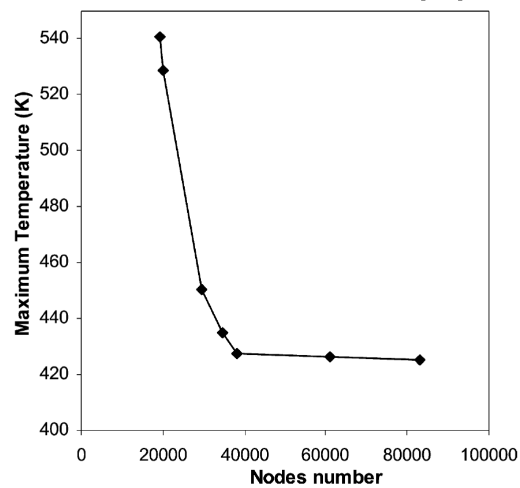

Figure 2.13: Temperature distribution in the wave-shaped heater from (Figure 2.12) [44].

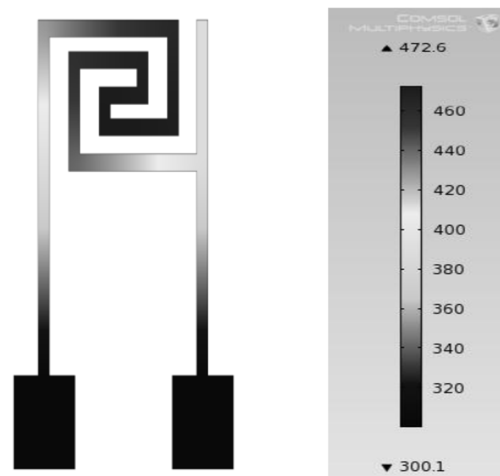

Figure 2.14: COMSOL simulation results for a spiral-shaped heater [43].

Chapter 3

Methodology And Results

This chapter is designed to outline the major parts of the experimental work completed and present the reader with the acquired results. First, I establish the groundwork of the project, outlining equipment, etching rates, and deposition method. I then present a rough chart of vanadium oxides in relation to deposition parameters. Sections 3.4.1 and 3.4.2 encompass the completed parametric studies and RF measurements that further improved the VO_2 deposition recipe. The chapter ends with a preliminary investigation into uniform localized micro-heating from a COMSOL model perspective.

3.1 Collaboration

The review stage of my research involved collaboration with two external groups. The first group aimed to perform reactive RF sputtering of VO_2 using a V_2O_3 target at low temperatures. The second group already had an established method based on the deposition of pure vanadium followed by annealing in a controlled oxygen environment. Neither of the cases produced samples adequate for RF application (as will be explained later), but they did allow me to deepen my experimental knowledge of the subject at hand.

Reactive RF sputtering using a V_2O_3 target is a valid deposition method, as discussed in the previous chapter. The desired deposition temperature for single-phase

VO_2 is in the 450℃-550℃ range. The system that was employed for the task was limited to 250℃ with the possibility of going up to 300℃ if the temperature stability was not of importance. The attempts of sputtering at such conditions were found to be unsuccessful. The low temperature deposition techniques presented in the review were then discussed, but due to an absence of a pure vanadium target for nucleation and the system being incapable of substrate biasing, the experiment was discontinued.

Deposition of VO_2 using pure vanadium and then followed by annealing in O_2 is a classic method of VO_2 deposition, as described in the literature review. The group that employed it did not have the equipment needed for the evaluation of the thoroughness of the vanadium oxidation. As a result, a thin under-layer of pure vanadium was found under most VO_x films prepared this way, thus impeding the switching performance of the devices. Overall, the approach was found to be limited to a film thickness of about 150 nm. This was sufficient for the optical applications of the research group that was employing it, but not adequate for RF use.

Overall, this experience had provided me with enough knowledge to approach the deposition of VO_2 myself. It has also taught me that the axiom ”do not give up” is a very important resolve to have as a graduate student.

3.2 Equipment

These subsections present the list of equipment utilized at various stages of the project and can be used as a reference in latter parts of the thesis. It also provides some general operational and process information.

VO_x Deposition

VO_x films were deposited using a twin chamber AJA ATC Orion Series sputtering system (Figure 3.1a) equipped with a 2” vanadium target, a quartz lamp substrate heater, and an RF-powered gun. The reason for using RF sputtering over DC is to avoid target poisoning during reactive oxide deposition. The general system parameters are: 78 mm substrate to gun distance, maximum deposition power of 200 W,

operating pressure of 3 mTorr and Ar flow of 27 STPT.

The deposition procedure involved heating the substrate to the desired temperature while waiting for the chamber to pump down below 1.8E-6 Torr. Heating to above 400℃ resulted in a large amount of outgassing, so a wait time of 10 min was implemented. Once the desired pressure and temperature were reached, the target would be started at 50 W, 30 mTorr of Ar/O2 mix and then ramped up to 200 W at 2W/sec. The shutter was kept closed for the first 2 min to prime the target. The system is not equipped with a cooling block, so samples were left inside the chamber until the temperature dropped below 50℃, which took about half an hour. For more process information, refer to Figure 3.5. The vanadium target was found to flake during depositions, necessitating regular cleaning.

VO_x Patterning

Lithography was completed using a spin coater, SUSS MicroTec MJB4 Mask Aligner and AZ330 positive PR. About 2 um of PR was deposited using the spinner, followed by: a 1 min prebake at 110℃; 4 sec exposure; 1 min postbake at 110℃; 2 min puddle development; and 1 min dehydration bake at 110℃.

Etching was done using AJA ATC-2030-Ionmill and a Cr etchant. The lowest power setting of the ionmill was employed due to hardening of the PR. Higher settings reinforced the PR to the point where it was difficult to remove. Cr etchant was found to be very effective as well, thus giving options of dry and wet approaches, depending on requirements.

Gold

A gold layer utilized for RF devices was deposited and patterned in accordance with the UW-MEMS procedure designed by CIRFE. For more process information, refer to Figure 3.5.

Analysis

Thickness measurements were done using a VEECO profilometer. The RF measurements of the devices were performed using a Cascade Microtech Model 9000 Manual RF Probe Station in conjunction with a vector network analyzer (VNA) (see Figures 3.1b and 3.1c). The initial XRD measurements were completed externally with the assistance of Professor Guo-Xing Miao.

3.3 Initial Work

The phase of the VO_x[1] deposited depends on the oxygen background in the chamber. After evaluating the literature, I decided that it would be prudent to start this experiment with a wide sweep (2%-12.5%) of partial oxygen flows, y, as defined in (3.3.0.1), where Q_{O_2} is the oxygen flow into the chamber and Q_{Ar} is argon flow at the gun, both measured in STPT.

$$y = \frac{Q_{O_2}}{(Q_{O_2} + Q_{Ar})} \tag{3.3.0.1}$$

Depositions were carried out at 450 ℃ for 20 min each. The main purpose of this run was to create a rough map of vanadium oxides, identified using XRD analysis. The samples also underwent a rudimentary transport measurement using a multimeter at room temperature and at 100℃. In the end, films were deemed to be of no more use and were utilized to test ionmill etching recipes.

The sample deposited at 10% partial oxygen flow was found to be the closest to VO_2 stoichiometry. The overall results are summarized in Table 3.1 with supporting XRD data presented in Figure 3.2. A clean alumina wafer was scanned for a reference signal, which was then subtracted from the acquired data. Nevertheless, the alumina background signal is still very strong due to the film thickness being below 100 nm. This claim will be supported in the deposition rate study, section 3.4.2. None of the samples are single-phase but are more of a combination of multiple vanadium oxides.

[1] The samples prepared over the course of my research are mixes of multiple vanadium oxides, thus I use the term of VO_x to distinguish them from pure single phase VO_2

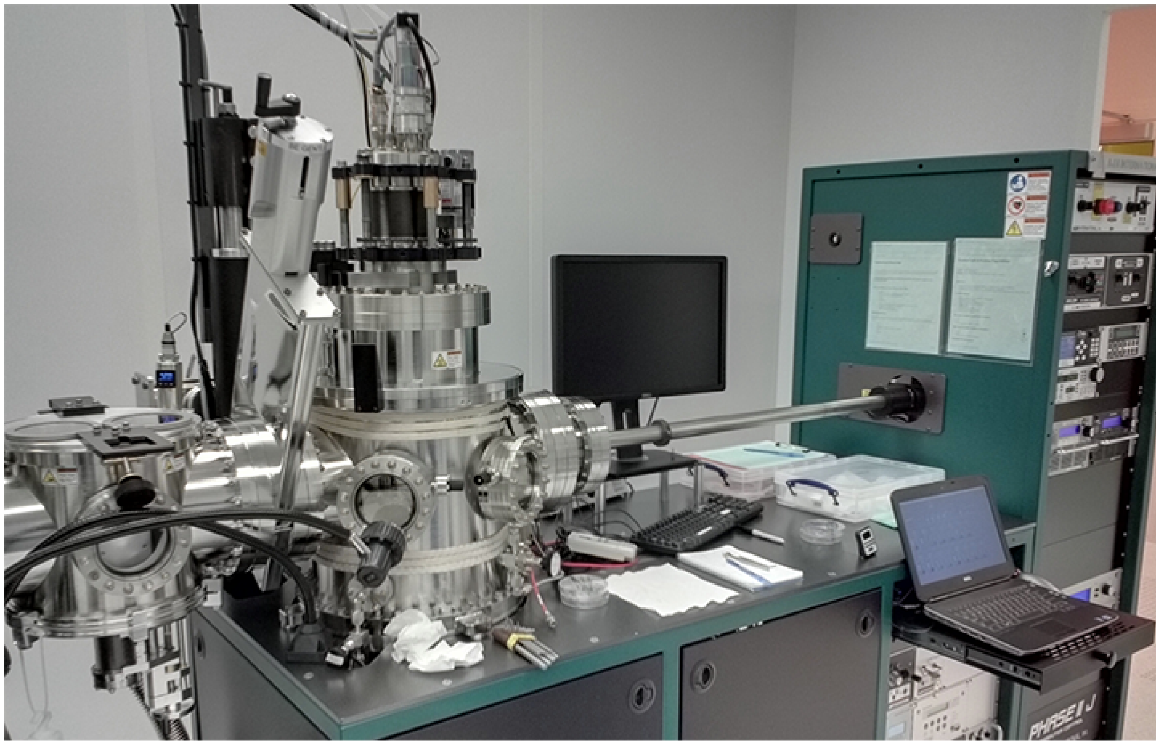

(a) Metals deposition chamber of the twin chamber AJA ATC Orion Series sputtering system

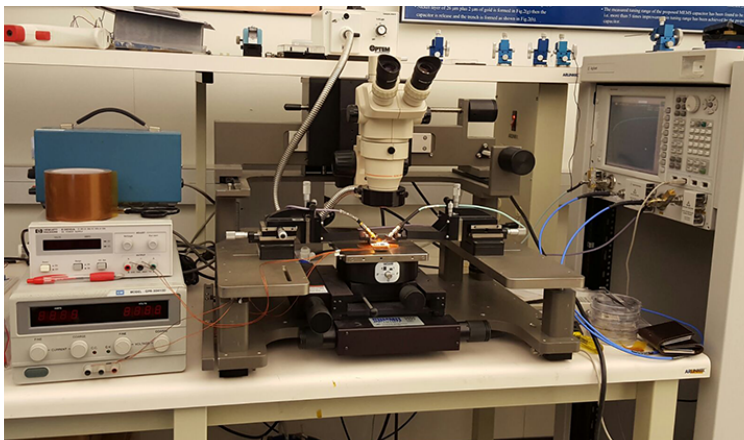

(b) Cascade Microtech Model 9000 Manual RF Probe Station setup

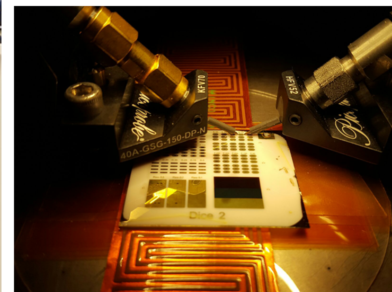

(c) A close-up of a sample wafer during RF analysis with a heater underneath, which is used to control the operating temperature of devices

Figure 3.1: Equipment

Based on the VO_2 peak in Figure 3.2b at 27°, it can be concluded that VO_2 is present in trace amounts and crystal grains are quite small due to the large breadth of the sample peak.

The purpose of the multimeter test was to confirm the XRD measurements. The samples were placed on a hotplate and evaluated at room temperature, followed by a 100℃ measurement. Only resistance across the 10% film was found to be affected by the temperature change, which is in agreement with the previous conclusion of it containing trace amounts of VO_2.

Table 3.1: VO_x chart in accordance to partial oxygen flows during deposition

O_2(STPT)	O_2(%)	Color	Dominant Oxide
0.6	2.2	Grey	–
1.42	5	Grey	–
2.19	7.5	Blue	V_2O_3
3	10	Blue-Green	VO_2
3.86	12.5	Green	V_2O_5

The ionmilling recipe development was accompanied by a secondary ion mass spectroscopy (SIMS) end-point detection and the profilometer thickness study. The two ions monitored for were vanadium, due to the content of the film, and aluminum, due to the content of the substrate. An AZ330 positive PR was used as the masking material. The system came with multiple presets referred to as Power Settings. In order to prevent the PR from burning, only two lowest settings were found acceptable, namely Power Setting 1 and Power Setting 2.

Sample SIMS data is demonstrated in Figure 3.3 and calculated etching rates are presented in Table 3.2.The sinusoidal noise present in the SIMS data is due to the sample stage rotation. The background count for aluminum is much stronger than for vanadium due to aluminum sample holder. The vanadium count drop slightly precedes aluminum count increase and thus can be used as a first sign of the etch being near completion. According to the data, Power Setting 2 is more advantageous, as it provides faster rates while allowing for thinner masking. Unfortunately, the PR on samples which underwent the etch at higher power was found to be reinforced

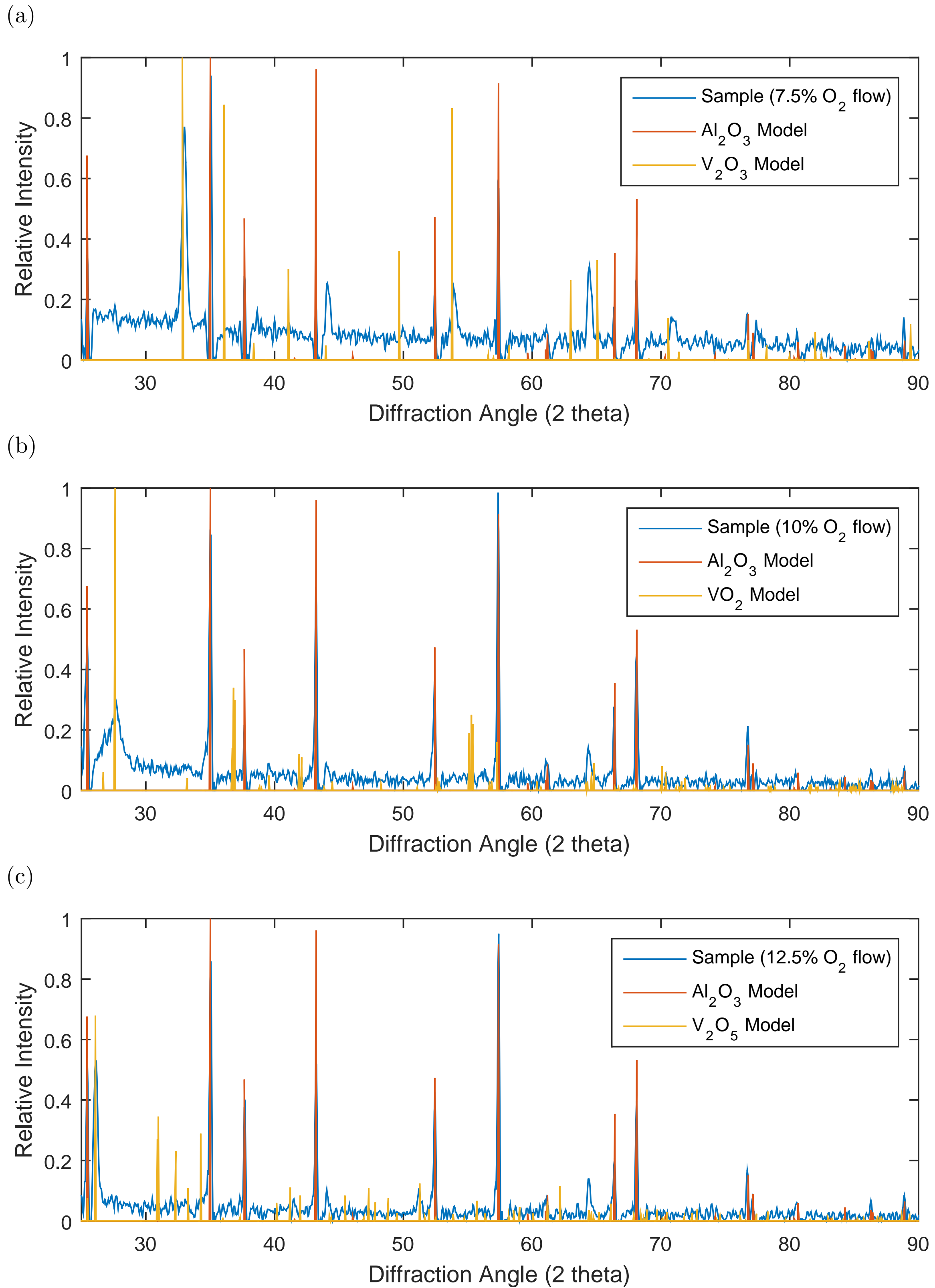

Figure 3.2: XRD patterns of VO_x films at various oxygen flow ratios. (a) 7.5% (b) 10% (c) 12.5%

by Ar bombardment, thus making it very resilient to PR stripping techniques. The samples were ultrasonically treated for 10 min in an acetone bath in an attempt to remove the reinforced PR, but some residue was still present after the treatment. Unless a different masking material is used, only Power Setting 1 can be utilized in this process.

Table 3.2: Ionmill etching rates for VO_x

	Power Setting 1	Power Setting 2
VO_x Etching Rate (nm/min):	9.5	23.8
AZ330 Etching Rate (nm/min):	55.8	116
$AZ330/VO_x$ Ratio:	6	5
Angle:	30°	30°

Even though VO_2 is not on the official list of materials etched by a Cr etchant, it was suggested that I give it a try. The undiluted[2] etching speeds were found to be very aggressive, with the rate being close to 30 nm/min. A Cr etchant is especially advantageous for this project, since it is known for not targeting Au, a material widely used in RF microfabrication.

3.4 Parametrics

At this point, samples with trace amounts of VO_2 exhibiting a clear MIT were obtained. To further improve the recipe, the characterization of VO_x performance was shifted to device level. A layout with a coplanar waveguide (CPW) series and parallel switches as well as series DC switches was prepared. For the full list of devices, please refer to Figure 3.7. In order to keep the fabrication process more manageable, I decided to use a bi-layer structure for initial devices, with Au signal/ground lines and VO_x as the switching material. Device-level heating can be incorporated in the future[3], but for the time being it was done globally by heating the entire wafer (Figure 3.1c). As mentioned previously, the main way to control which phase of vanadium

[2] In this experiment, the Cr etchant was used as is, but it is a common practice to dilute the etchant if more control is required.

[3] The last section of the chapter provides the preliminary investigation of the localized heating.

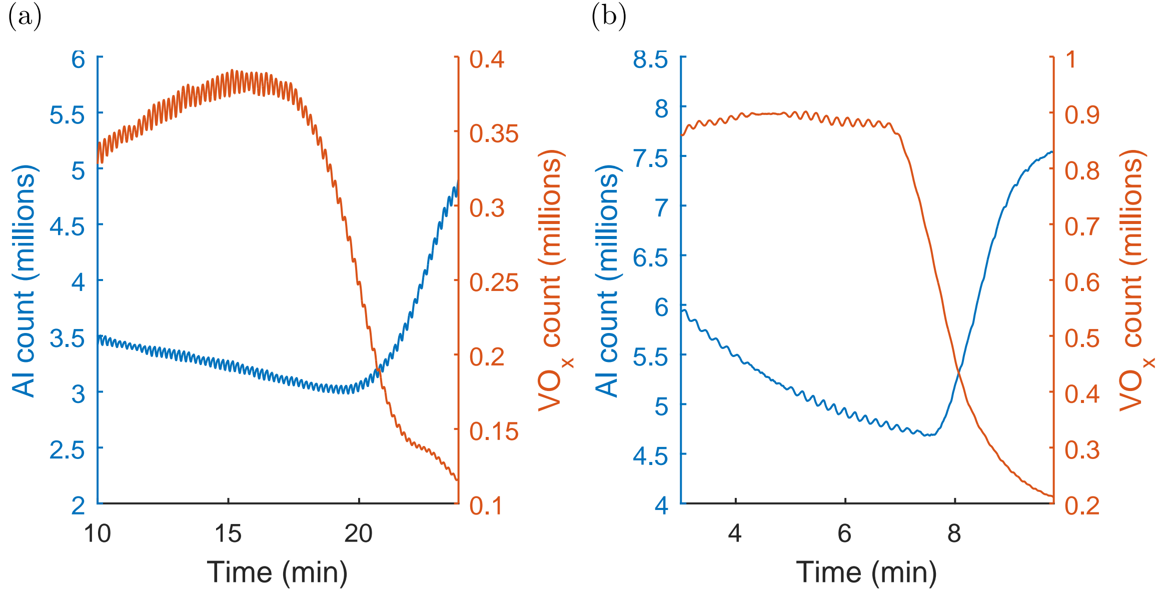

Figure 3.3: Sample SIMS data for VO_x etching process using ionmill. (a) Power setting 1 (b) Power setting 2

oxide is deposited is via oxygen flow, thus making a parametric study of oxygen flow essential for this project.

Before moving on, I would like to provide a justification for the use of series switches with 5 um gap and S_{21} parameter measurements exclusively. At the current state of the project, VO_x deposited is still a very poor conductor even at high temperature, resulting in series switches exhibiting very high insertion loss. The devices designed are 2-port and are matched to 50Ω, so the S_{21} parameter measured can be treated as insertion loss. A series switch with the shortest gap (assuming that port isolation is retained) will provide the highest contrast if the VO_x deposited is closer to single-phase VO_2. An argument can be made for the use of parallel switches with very wide VO_x short from signal-to-ground and reflection coefficient measurements based on S_{11}.

3.4.1 Partial Oxygen Flow Parametric Study

For a high quality parametric study, it is important to minimize the number of variables. The full fabrication process utilized is presented in Figure 3.5, with 8 steps

dedicated to the Au layer and the last 4 to VO_x layer. Given that the focus of this project is VO_x, I have isolated its deposition from the rest of the process by introducing a 4x die mask (Figure 3.4) for Au layer fabrication. The idea behind this is to fabricate 4x copies of the Au layout on a single wafer, which is then diced into 4x identical quarters and utilized for parametric studies of VO_x. This approach provides me with a solid baseline, and allows me to state that the main difference between two identical devices on two separate dies is the VO_x layer.

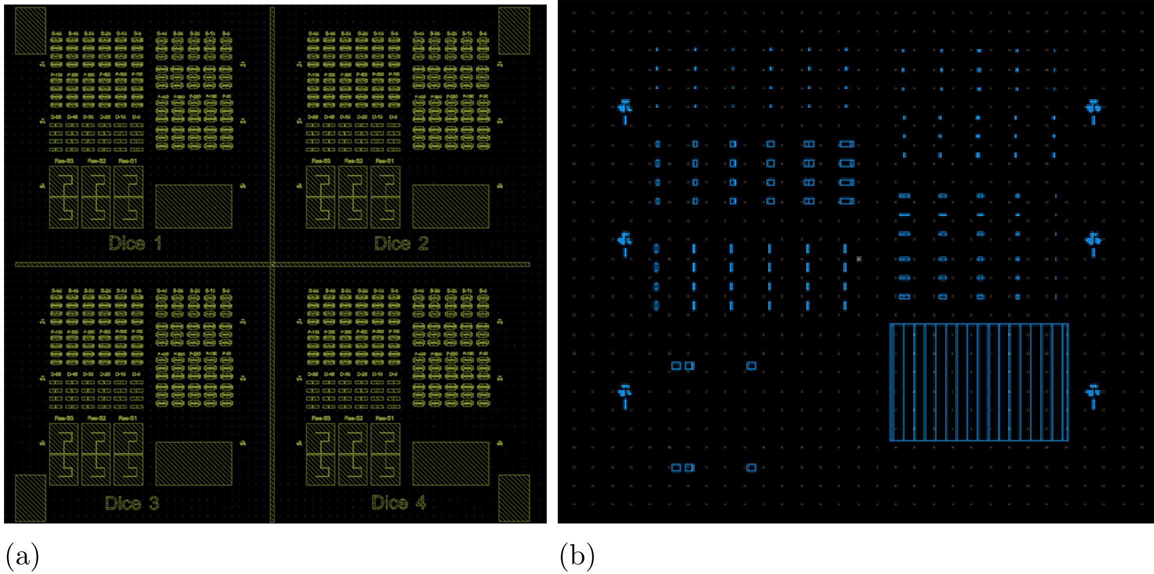

(a) (b)

Figure 3.4: Masks used for (a) Au patterning and (b) VO_x patterning

For the first parametric study, VO_x films were deposited at partial oxygen flows ranging from 10.25% to 11%. A rough 25 mil amorphous alumina wafer was used as the substrate. I have increased the substrate temperature during the deposition to 500℃ in order to promote larger crystalline grains. The deposition time was about 30 min. Due to the extreme roughness of the substrate, it was impossible to determine the thickness of the films using a profilometer. However, based on data obtained later, it was deduced that the thickness was close to 50 nm. The S-parameter measurements were completed using VNA (Figure 3.1b) with wafers at room temperature ("cold") and at 100℃+ ("hot").

The wafers were cross-compared based on the insertion loss of CPW series switches with 5 um gap, which were chosen over other devices due to previously stated jus-

tifications. S_{21} results are presented in Figure 3.6a. The switching ratio[4] of the device increased with the reduction of partial oxygen flow, with the device fabricated at 10.25% performing the best. Besides thermoelectric switching, thermochromic switching was also observed, with the color of the VO_x film changing from blue to green when heated.

The parametric study of VO_x dependence on partial oxygen flow was continued with a second run, with flows ranging from 10.2% to 9.8%. Due to the extreme roughness of the previously used substrate, a smooth 11 mil amorphous alumina wafer was utilized for this study, thus allowing for film thickness measurements. Substrate temperature and deposition time were kept constant at 500℃ and 30 min, respectively.

The wafers were analyzed in the same manner as in the previous study. S_{21} results are presented in Figure 3.6b. It is clear that switching is not as aggressive at higher frequencies, which was expected due to the thinner substrate. Film switching capabilities are very low in samples deposited below 10% partial oxygen flow, which leads one to conclude that optimal deposition conditions are around 10.2%-10.25%. Once again, all three samples demonstrated chromatic switching from blue to green, with the exception of the sample deposited at 9.8%, which changed from golden to green. The thickness of the first two films was found to be just below 50 nm, while the third film was closer to 75 nm.

The purpose of the final partial oxygen flow study was to determine if the behaviour of the films is consistent with increase in deposition time. An 11 mil wafer was utilized once again, with a deposition time of 90 min and a substrate temperature of 500 ℃. The partial oxygen flow was adjusted between 10.3% and 9.4%.

The RF performance of the devices relative to each other was similar to the previous studies. S_{21} results are presented in Figure 3.6c. The thickness of the 10.3% sample is 136 nm, while the other two are closer to 230 nm. The chromatic behaviour of the samples did not change, with the exception of darker shades of color, which can be attributed to the increased thickness of the films.

[4] The difference in insertion loss of the device at room temperature and at 100℃+

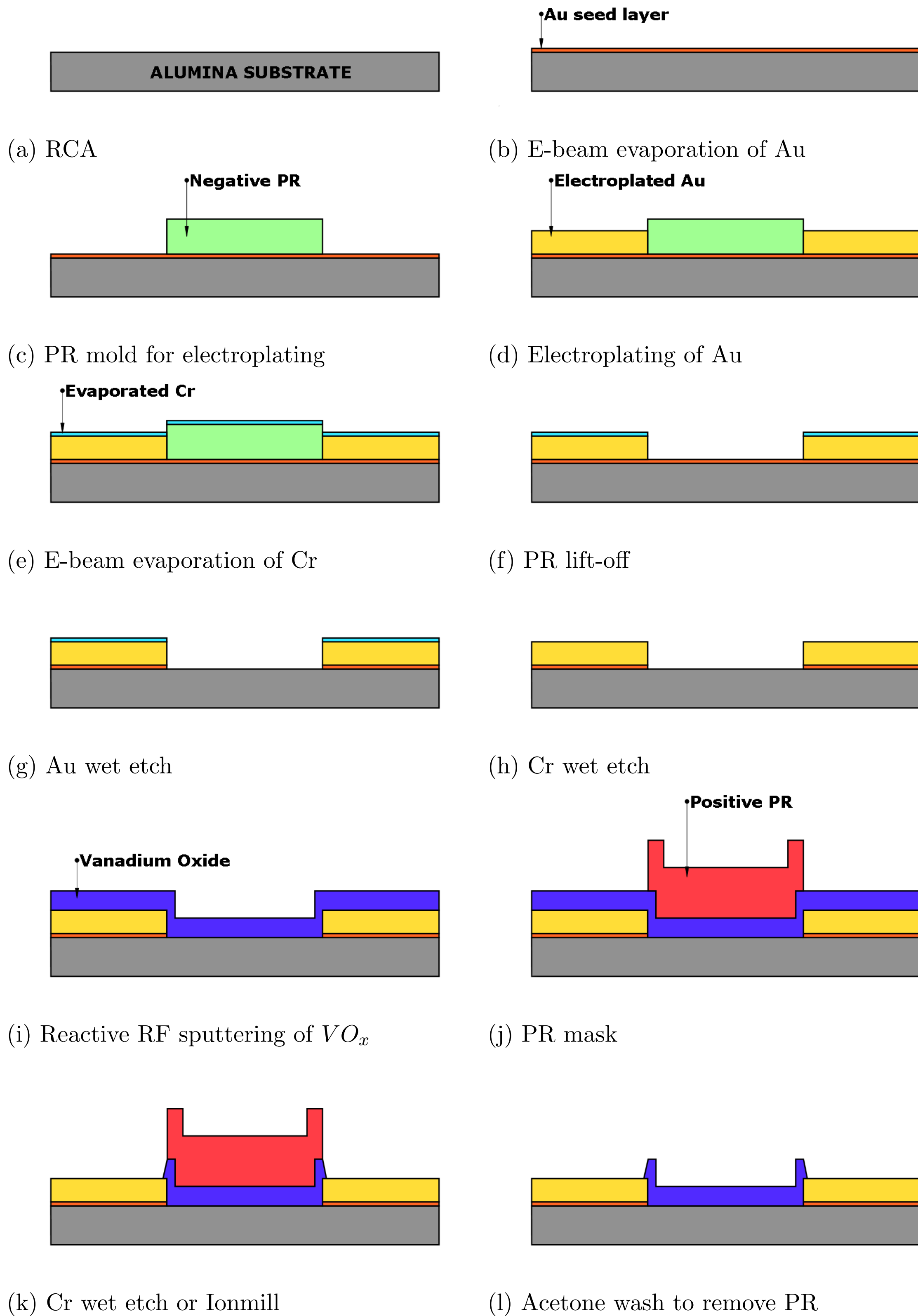

(a) RCA
(b) E-beam evaporation of Au
(c) PR mold for electroplating
(d) Electroplating of Au
(e) E-beam evaporation of Cr
(f) PR lift-off
(g) Au wet etch
(h) Cr wet etch
(i) Reactive RF sputtering of VO_x
(j) PR mask
(k) Cr wet etch or Ionmill
(l) Acetone wash to remove PR

Figure 3.5: General process for device microfabrication used in this project

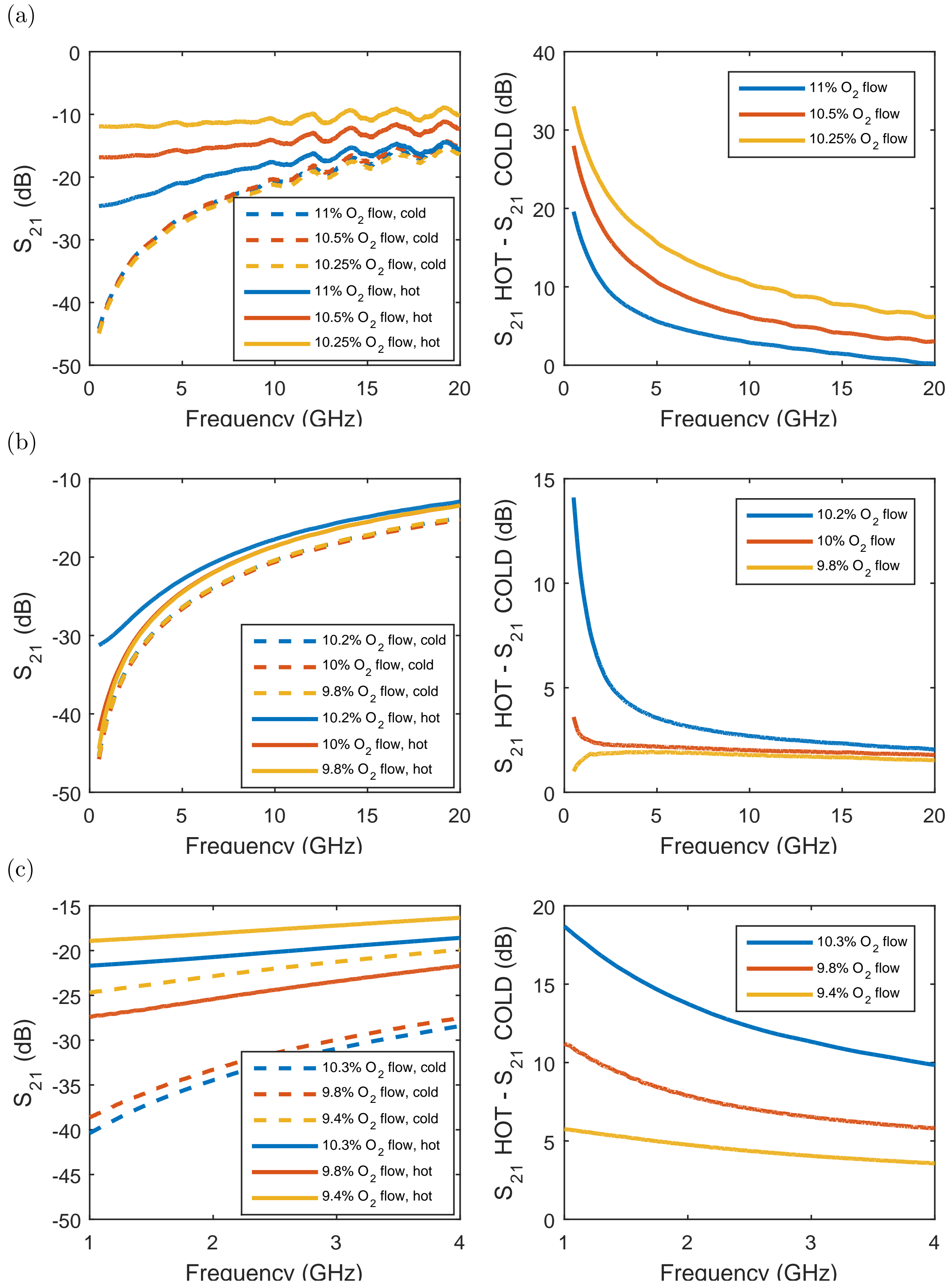

Figure 3.6: S_{21} analysis of partial oxygen flow studies. "hot" refers to 100℃+ and "cold" refers to room temperature. (a)11%-10.25% (b)10.20%-9.8% (c)10.3%-9.4%, much thicker films

Figure 3.7: Fabricated devices included in the mask layout for this project. The number above the device defines the size of the gap or the width of the short in um. (a) DC switches with variable gaps (b) CPW series switches ver1, with variable gaps (c) CPW parallel switches ver1, with variable shorts (d) CPW series switches ver2, with variable gaps (e) CPW parallel switches ver2, with variable shorts.

3.4.2 Deposition Rate and Temperature Studies

The deposition rate of the VO_x is a topic of interest to this project, so I have evaluated its dependence on deposition time, partial oxygen flow, and substrate temperature. The database used for this study is a combination of data collected during previous experiments as well as some supplementary depositions. The initial decision was to keep two out of three parameters constant while performing three separate evaluations, but the results showed that it does not need to be the case.

The first study was aimed at evaluating if deposition rate is constant with time. The partial oxygen flow and substrate temperature were fixed at 9.8% and 500℃, respectively. According to the literature, the non-linear region of the deposition should be well below the minimum deposition time of 30 min used in this project. The results are presented in Figure 3.8b, showing that the R-squared value of the linear regression is 1. It can be concluded that the deposition rate is unaffected by the duration of the deposition in the context of this project.

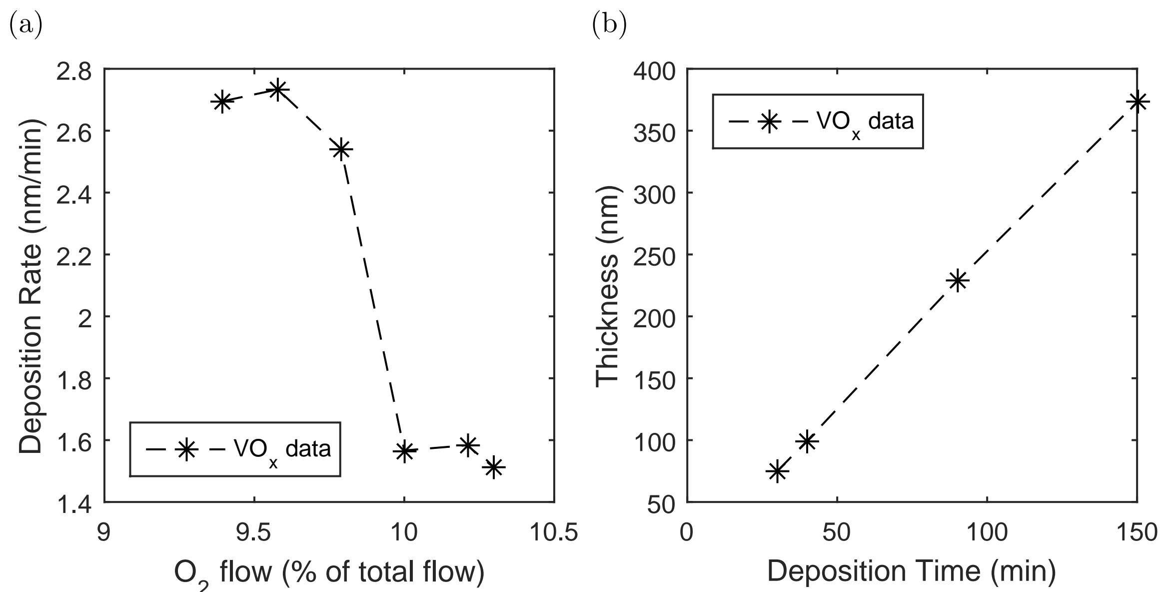

Figure 3.8: Deposition rate behaviour with (a) change in partial oxygen flow and (b) time

The second study of this section is based on the effect of partial oxygen flow on the deposition rate. In light of the conclusion presented in the previous study, I decided to increase the data pool by using 30 min samples as well as 90 min, 115 min and

150 min samples. It was shown by other research groups that the sputtering rate drops drastically when entering the VO_2 region of the deposition (Figure 2.7) [23]. My results are presented in Figure 3.8a and are consistent with this observation. The target was monitored for oxygen poisoning. Table 3.3 shows that it was not the case, as otherwise a distinct change in voltage and power at the target would have been observed.

Table 3.3: Power and voltage response to oxygen flow change, at the target of the sputtering system

O_2 set (STPT)	O_2 read (STPT)	Power (W)	Voltage (V)
2.8	2.78	199	226.5
2.85	2.82	199	225
2.9	2.87	199	225
2.95	2.92	198.5	225.5
3	2.97	198.5	224.5
3.05	3.02	198	225
3.1	3.07	198	225.5
3.15	3.12	198	225

Lastly, the effects of the substrate temperature during the deposition were evaluated. Three samples were deposited at temperatures of 400℃, 500℃, and 550℃. The deposition time and partial oxygen flow were kept at 40 min and 9.8% respectively. The thickness of the films and the device performance were evaluated using profilometer and VNA. The deposition rate data presented in Table 3.4 is somewhat inconclusive. S_{21} data for a CPW series switch with 5 um gap is plotted in Figure 3.9.

Table 3.4: Dependence of deposition rate of VO_x on substrate temperature

Substrate Temperature (℃)	Deposition Rate (nm/min)
550	2.46
500	2.50
400	2.37

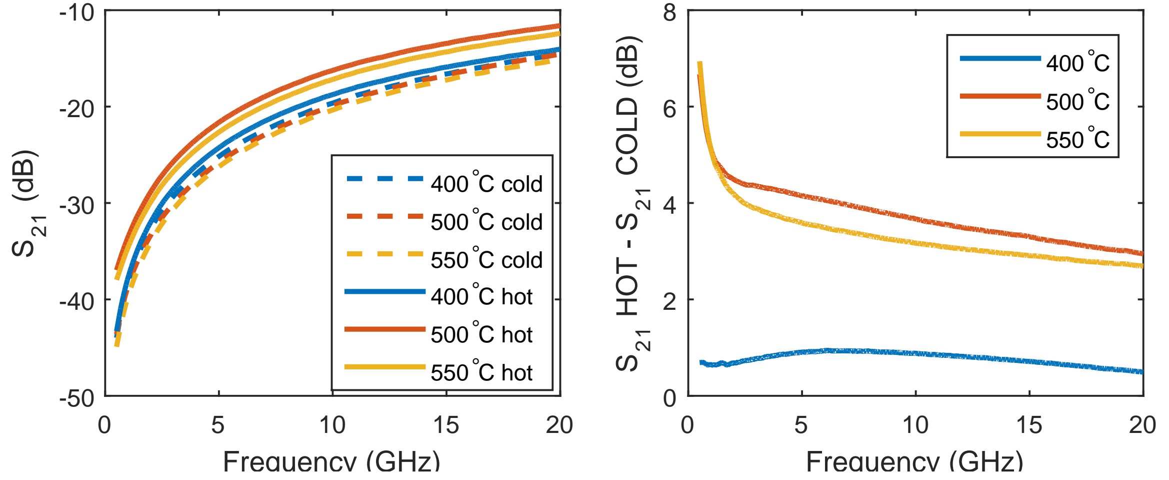

Figure 3.9: S_{21} analysis of samples deposited at variable substrate temperatures

3.5 Heating

Considering the thermoelectric nature of RF switches presented in this project, a localized heating solution will be required at some point in the future. Two types of coil micro-heaters were reviewed earlier in this paper, spiral and wave. The main issue with coil heating is the so-called hot spot formation, when the temperature at the center of the heater is much higher than at the extremities. It is common practice to adjust the line thickness, thus producing less resistance in the middle of the structure and leading to a drop in Joule heating. This is especially true for spiral heaters but can be difficult to implement in wave heaters. In the latter type, most of the lines are single directional, so the line width correction tends to stretch out the hot spot in the corresponding direction instead of fully eliminating it. In this section I will provide my approach to bi-directional correction of the hot spot in wave-shaped heaters.

The model was constructed using COMSOL MATLAB LiveLink (the script is attached in Appendix A. Heat Transfer in Solids (ht) and Electric Currents, Shell (ecs) modules were utilized. Heater and substrate materials were Cr and amorphous alumina, respectively. It was assumed that the heater would undergo convective cooling by air during its operation and lose heat to the substrate. The task of correcting the hot spot was split into two parts: horizontal and vertical. The width of the coil lines underwent a parabolic correction, with the lines on the inside being thicker than those

on the outside. This approach resulted in stretching out the hot spot as mentioned previously. On the vertical side of things, I introduced corrugations which periodically reduce the resistance of the line, with longer corrugations being in the middle. This reduced its resistance from a vertical perspective.

Figure 3.10a provides a sample layout of a 250 um x 550 um heater with both hot spot corrections implemented. Figure 3.10b demonstrates the temperature distribution immediately below the surface of the substrate and also provides a map of cross-sections displayed in Figures 3.10c and 3.10d. Horizontal correction was found to be much stronger than vertical correction, which can be utilized for 1D heating elements like Figure 3.10e. The resulting temperature cross-section is plotted in Figure 3.10f. Although vertical correction demonstrated a visible improvement, it was not as significant as the horizontal one.

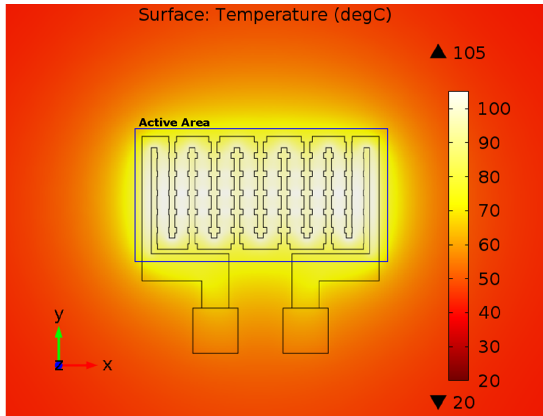

(a) Layout of a 250 um x 550 um microheater with surface temperature distribution

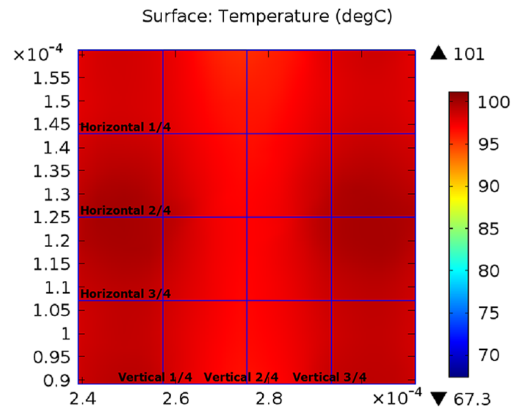

(b) Temperature distribution of the active area in (a), 6 um under the surface of the substrate

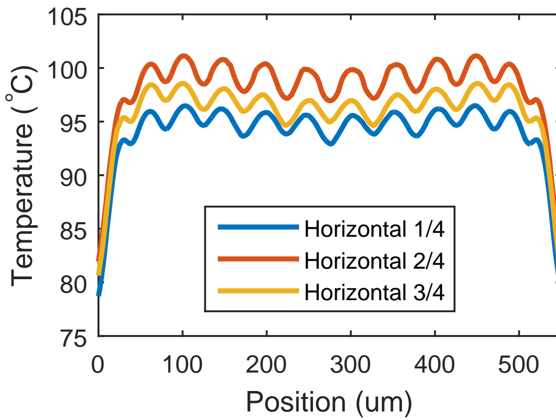

(c) Horizontal temperature distribution cross-sections of the active area shown in (a) and (b), line width "hot spot" correction

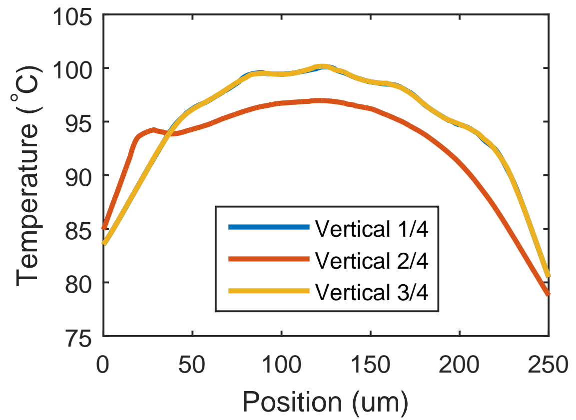

(d) Vertical temperature distribution cross-sections of the active area shown in (a) and (b), corrugation "hot spot" correction

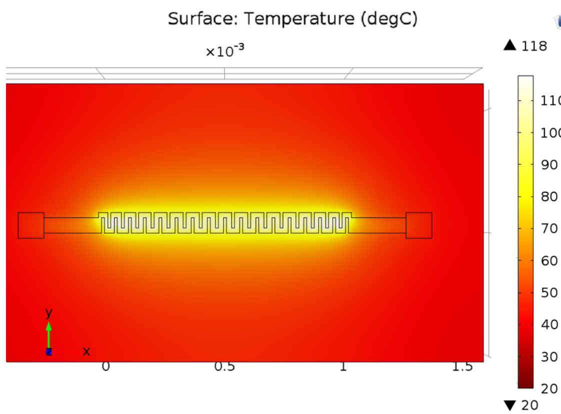

(e) An example of a heater with a high aspect ratio, 1000 um x 60 um, with a surface temperature distribution

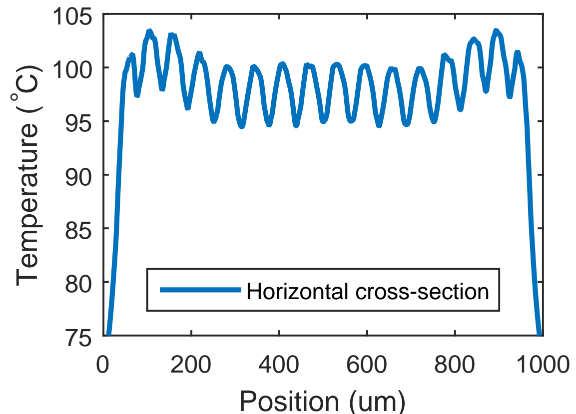

(f) Horizontal cross-section temperature distribution of the heater demonstrated in (e)

Figure 3.10: Custom design of a wave-shaped micro-heater

Chapter 4

Discussion

This project was designed to be a stepping stone into polycrystalline VO_2 research for the University of Waterloo and more specifically for the CIRFE research group. In this chapter, I will discuss the current state of the microfabrication process as well as improvements in the VO_x performance and localized micro-heating. I will then conclude my current finding and provide suggestions for the project's future direction.

Microfabrication Process

The main limiting factor that I faced when locating equipment suitable for VO_2 deposition was substrate heating. The majority of the reviewed methods require deposition temperatures of 400℃ and higher. The only system that I found available for my use was the twin-chamber sputtering setup, located at Quantum NanoFab Facilities. The quartz lamps used for the substrate heating in the system were capable of achieving the required temperatures and higher. The only setup-related issue that arose closer to the end of the project concerned the VO_2 deposition rate. The system was designed for use with 2" targets. In order to increase the output, a larger target or multiple targets were required. The RF power supply of the system was not capable of supplying 2x targets with 200W, thus an additional power supply was needed for co-sputtering. Furthermore, using larger targets would require an RF gun setup redesign, which is a solid but complex solution.

The task of patterning VO_x was approached using ionmilling as well as wet etching with a Cr etchant. The latter method demonstrated faster etching rates and better selectivity, both of which are important qualities. However, it also resulted in a residue formation on top of revealed gold surface, visible in Figure 3.7. A Cr etchant does not target gold on its own, so it can be assumed that the cause of the residue was the VO_x/Au interface. Although the residue has not led to any loss in performance at the current stage of the project, it might impede the deposition of additional layers in the future. As an option, a barrier layer of Cr can be introduced between Au and VO_x. Such a modification is rather simple, as all it requires is the removal of step (h) in Figure 3.5 from the process. As a result, the barrier layer will be removed with unwanted VO_x during the final Cr wet etch, thus preventing the majority of the VO_x/Au interface.

VO_x Thin Film Behaviour and Improvements

It was previously stated that the two main parameters for reactive RF sputtering of VO_2 are substrate temperature and partial oxygen flow. Vanadium is capable of forming multiple stable oxides, six of which are located in the deposition region of interest: V_2O_3, V_4O_7, VO_2, V_6O_{13}, V_3O_7 and V_2O_5 (Figure 2.8). Higher temperature deposition tends to favour single-phase formation and produce larger crystalline grains, with a trade-off of increased roughness. In order to achieve a true single-phase of VO_2, very precise control over oxygen flow is required. It was demonstrated that a difference of 0.25% in partial oxygen flow from optimal conditions can lead to an increase of several dB in insertion loss and a drop in switching ratio. In the oxygen flow parametric study, I found that 10.2%-10.3% partial oxygen flow range was most favourable for VO_2 growth. In terms of deposition temperature, a sample deposited at 500℃ outperformed the sample deposited at 400℃. Considering that the thickness of the samples was identical, it can be concluded that the improvement is purely material related. On the other hand, when the 550℃ sample was compared to the 500℃ one, the behaviour is somewhat unnatural. According to the literature, a marginal improvement should be expected, but there was a clear increase in insertion loss at

higher frequencies. Once again, the thicknesses of the samples were identical, so the effect must have been material-based as well. The temperature study results were inconclusive and more sampling at higher deposition temperatures is required.

The deposition rate of VO_x drops by a half at the 9.8% partial oxygen flow mark, thus creating an edge which separates conductive oxides from non-conductive ones. According to the literature, the optimal deposition condition is located at the lower part of the edge, while the suggested flows of 10.2%-10.3% are slightly past the edge. This inconsistency might be due to the fact that the edge is not yet fully mapped out. For the higher oxygen flow study, rough wafers were utilized. Hence, the thickness of the films deposited is unknown and might be less than estimated. A repeat of the depositions on a smooth substrate should provide data needed to advance the current state of the study. The deposition rate at 9.8% is constant with time, and thus I made an assumption that this stands true for all other oxygen flow rates. It was also demonstrated that the performance of films relative to each other does not change with thickness, and that the insertion loss cross-comparison of thicker samples mirrored that of thinner ones. One of the goals of the project was to deposit a 300 nm film of VO_2, which can be achieved with a 3 hour deposition at 10.2%-10.3% partial oxygen flow. Considering that the equipment requires constant supervision, the process is too long to run solo, hence the previous suggestions for increasing the deposition rate. An obvious alternative would be to introduce a second person to supervise the equipment during deposition.

As previously reviewed, the fact that VO_2 MIT occurs near room temperature makes the task of localized heating somewhat similar to that of MEMS sensors, where coil heaters are often implemented. In my work I have presented a design for a wave-shaped heater with duel hot spot corrections. It is common practice to alter the widths of coil lines, which I did to correct the temperature distribution horizontally. The innovation lies in the corrugations, which I introduced as a vertical hot spot correction method. The results were an improvement; specifically the hot spot was more stretched out vertically than without corrugations. However, further work is required. The corrugations do not drop the line resistance sufficiently, so I suggest in-

troducing a third dimension to them. The alteration of corrugation thicknesses can be incorporated into contact fabrication for the heater, thus keeping the microfabrication process identical.

4.1 Conclusion

The process of reactive RF sputtering of the VO_x developed can be combined with the gold microfabrication process practiced at CIRFE with very minor changes, simplifying the procedure. The optimal deposition parameters were found to be 500℃ substrate temperature, 3 mTorr chamber pressure, 27 STPT Ar, and 10.2%-10.3% O_2. The deposition rate at these conditions is close to 1.5 nm/min. A design for future localized heating has been provided, but requires experimental testing and further improvements.

The main goal of my research was to fabricate a 2-port series RF switch with 30 dB isolation in the OFF state and 1 dB insertion loss in the ON state. Figure 3.6c demonstrates the insertion loss behaviour of a sample that was deposited at 10.3% partial oxygen flow, 500℃ substrate temperature, and 90 min deposition time. The isolation is over 30 dB at all measured frequencies, while the ON state insertion loss is less than 22 dB. This observation concludes that even optimized VO_x recipe does not yet deposit films of sufficient purity. That said, I do believe that the quality of VO_x deposited using the sputtering system employed can be further improved. For the next phase of the project, I would suggest performing a more detailed parametric study in the 10%-10.5% partial oxygen flow range. I would include scanning electron microscopy (SEM) measurements for texture and topography evaluation, and XRD to compare the current state of films relative to the ones at the beginning of this project.

In addition to the changes suggested above, I would also redesign the RF measurements rig. The current setup does not provide much in terms of temperature control. This can be greatly improved by acquiring a temperature controller with thermocouples and a cooling block. Such a setup would allow for observation of hysteresis from

an RF perspective, which would be highly beneficial for the characterization of the material.

Appendix A

Micro-heating

COMSOL MATLAB LiveLink script for generating wave-shaped micro-heater model with "hot spot" corrections

---

```
clearvars % clear variables

ModelUtil.remove('model') % loading the model
ModelUtil.clear

model = mphload('ver1_5.mph')

ref = 10 % precision for finding horizontal and vertical fitting factors
ref_sec = 15
same_side = 1 % contacts on the same side (1) or on opposite sides (0)
volt_scan = 0

B_w_min = 25; % minimum and maximum width of vertical coil lines in um
B_w_max = 90;

B_l_min = 25; % minimum and maximum width of horizontal coil lines in um
B_l_max = 110;

const_bar_x = 0; % it possible to keep width of a certain number of
   vertical or horizontal lines constant
const_bar_y = 0;

VOx_w = 1000; % size of the area needed to be heated
VOx_l = 1000;
v_fac = 1000;
h_fac = 1000;

min_spx = 15; % minimum horizontal and vertical spacing between lines
min_spy = 8;

bar_w = 75; % initial bar width
```

```
contact_size = 100; % contact, size, spacing, distance and connecting line
   width
contact_spacing = 100;
contact_distance = 160;
contact_line_width = 60;

sub_thickness=1000; % substrate thickness, distance from the heater to the
   border of the substrate, cr_thickness and applied voltage between
   contacts
sub_border = 500;
cr_thickness = 1;
applied_voltage = 10;

% The following script builds the model to the desired specifications

g1=model.geom('geom1');
wp1 = g1.feature('wp1');
e1 = g1.feature('e1');
g1.feature.remove('wp1');
g1.feature.remove('e1');
wp1=g1.feature.create('wp1','WorkPlane');

if (VOx_w/(B_w_max+min_spx))<const_bar_x*2
    const_bar_x = 0;
end

if (VOx_l/(B_l_max+min_spy))<const_bar_y*2
    const_bar_y = 0;
end

total_width = 0;
tot_wbar = const_bar_x;
ref_flag = 1;
while (total_width < VOx_w)||(ref_flag<ref)
    tot_wbar = tot_wbar+1;

    if (const_bar_x ==0)
        xw = 0;
        xw = 1:1:tot_wbar;
    else
        xw=0;
        xw(1:const_bar_x)=1;
        xw((const_bar_x+1):tot_wbar) = 2:1:(tot_wbar-const_bar_x+1);
    end

    yw=round(-(xw.^2).*h_fac+(B_w_max+h_fac));
```

```
    total_width = (tot_wbar*min_spx+sum(yw))*2+min_spx;
    if yw(end) < B_w_min
        tot_wbar = const_bar_x;
        total_width = 0;
        h_fac = h_fac-(5*10^(-ref_flag));
    elseif (yw(end) >= B_w_min)&&(ref_flag<ref)&&(total_width > VOx_w)
        h_fac = h_fac+(5*10^(-ref_flag));
        tot_wbar = const_bar_x;
        total_width = 0;
        ref_flag = ref_flag+1;
    end

    if (h_fac <= 0)&&(ref_flag<ref)
        h_fac = h_fac+(5*10^(-ref_flag));
        tot_wbar = const_bar_x;
        total_width = 0;
        ref_flag = ref_flag+1;
    elseif (h_fac <= 0)&&(ref_flag==ref)
       display('H_FAC DROPPED BELOW 0')
       total_width = VOx_w;
    end
end


if (tot_wbar==1)&&(total_width >= VOx_w)
    yw = [fliplr(yw) yw];
else
    tot_wbar = tot_wbar-1;
    if (const_bar_x ==0)
        xw = 0;
        xw = 1:1:tot_wbar;
    else
        xw=0;
        xw(1:const_bar_x)=1;
        xw((const_bar_x+1):tot_wbar) = 2:1:(tot_wbar-const_bar_x+1);
    end
    yw=round(-(xw.^2).*h_fac+(B_w_max+h_fac));
    total_width = (tot_wbar*min_spx+sum(yw))*2+min_spx;
    while (total_width < VOx_w)
        min_spx = min_spx+0.1;
        total_width = (tot_wbar*min_spx+sum(yw))*2+min_spx;
    end
    yw = [fliplr(yw) yw];
end

bar_width = ((yw<bar_w).*yw)+((yw>=bar_w).*bar_w);
display(['h_fac was set at ' num2str(h_fac)])
```

```
total_length = 0;
tot_lbar = const_bar_y;
ref_flag = 1;
while (total_length < VOx_l)||(ref_flag<ref)
    tot_lbar = tot_lbar+1;

    if (const_bar_y ==0)
        xl = 0;
        xl = 1:1:tot_lbar;
    else
        xl=0;
        xl(1:const_bar_y)=1;
        xl((const_bar_y+1):tot_lbar) = 2:1:(tot_lbar-const_bar_y+1);
    end

    yl=round(-(xl.^2).*v_fac+(B_l_max+v_fac));
    total_length = (tot_lbar*min_spy+sum(yl))*2+min_spy;
    if yl(end) < B_l_min
        tot_lbar = const_bar_y;
        total_length = 0;
        v_fac = v_fac-(5*10^(-ref_flag));
    elseif (yl(end) >= B_l_min)&&(ref_flag<ref)&&(total_length > VOx_l)
        v_fac = v_fac+(5*10^(-ref_flag));
        tot_lbar = const_bar_y;
        total_length = 0;
        ref_flag = ref_flag+1;
    end

    if (v_fac <= 0)&&(ref_flag<ref)
        v_fac = v_fac+(5*10^(-ref_flag));
        tot_lbar = const_bar_y;
        total_length = 0;
        ref_flag = ref_flag+1;
    elseif (v_fac <= 0)&&(ref_flag==ref)
       display('H_FAC DROPPED BELOW 0')
       total_length = VOx_l;
    end
end

display(['v_fac was set at ' num2str(v_fac)])


if (tot_lbar==1)&&(total_length >= VOx_l)
    yl = yl*2+min_spy;
    total_length = yl+min_spy*2;
else
```

```
    tot_lbar = tot_lbar-1;
    if (const_bar_y ==0)
        xl = 0;
        xl = 1:1:tot_lbar;
    else
        xl=0;
        xl(1:const_bar_y)=1;
        xl((const_bar_y+1):tot_lbar) = 2:1:(tot_lbar-const_bar_y+1);
    end
    yl=round(-(xl.^2).*v_fac+(B_l_max+v_fac));
    total_length = (tot_lbar*min_spy+sum(yl))*2+min_spy;
    while (total_length < VOx_l)
        min_spy = min_spy+0.1;
        total_length = (tot_lbar*min_spy+sum(yl))*2+min_spy;
    end
    yl = [fliplr(yl) yl];
end

x_bars = yw*triu(ones(length(yw),length(yw)))+min_spx.*ones...
(1,length(yw))*triu(ones(length(yw),length(yw)))-yw./2-bar_width./2;
y_bars(1:2:(length(yw)-1))=total_length-bar_w;
y_bars(2:2:(length(yw)-1))=0;
y_bars_width = x_bars(2:end)-x_bars(1:end-1);

wp1.geom.create(['rw' num2str(0)],'Rectangle');
wp1.geom.feature(['rw' num2str(0)]).set...
('size',{num2str(min_spx*1e-6),num2str(total_length*1e-6)});
wp1.geom.feature(['rw' num2str(0)]).set('pos',{'0','0'});

for j=1:1:length(yw)
    wp1.geom.create(['rw' num2str(j)],'Rectangle');
    wp1.geom.feature(['rw'
        num2str(j)]).set('size',{num2str(min_spx*1e-6),...
    num2str(total_length*1e-6)});
    wp1.geom.feature(['rw' num2str(j)]).set('pos',{num2str((min_spx*j+...
    sum(yw(1:j)))*1e-6),'0'});

    wp1.geom.create(['vbar' num2str(j)],'Rectangle');
    wp1.geom.feature(['vbar' num2str(j)]).set('size',{num2str...
    (bar_width(j)*1e-6),...num2str(total_length*1e-6)});
    wp1.geom.feature(['vbar'
        num2str(j)]).set('pos',{num2str(x_bars(j)*1e-6),'0'});

    if j<length(yw)
        wp1.geom.create(['hbar' num2str(j)],'Rectangle');
        wp1.geom.feature(['hbar' num2str(j)]).set('size',...
        {num2str(y_bars_width(j)*1e-6),num2str(bar_w*1e-6)});
```

```
        wp1.geom.feature(['hbar' num2str(j)]).set('pos',...
        {num2str(x_bars(j)*1e-6),num2str(y_bars(j)*1e-6)});
    end
end

wp1.geom.create(['rl' num2str(0)],'Rectangle');
wp1.geom.feature(['rl' num2str(0)]).set...
('size',{num2str(total_width*1e-6),num2str(min_spy*1e-6)});
wp1.geom.feature(['rl' num2str(0)]).set('pos',{'0','0'});

for j=1:1:length(yl)
    wp1.geom.create(['rl' num2str(j)],'Rectangle');
    wp1.geom.feature(['rl' num2str(j)]).set('size',{num2str...
    (total_width*1e-6),num2str(min_spy*1e-6)});
    wp1.geom.feature(['rl' num2str(j)]).set('pos',{'0',num2str...
    ((min_spy*j+sum(yl(1:j)))*1e-6)});
end


wp1.geom.create('Box','Rectangle');
wp1.geom.feature('Box').set('size',{num2str...
(total_width*1e-6),num2str(total_length*1e-6)});
wp1.geom.feature('Box').set('pos',{'0','0'});

wp1.geom.create('substr','Rectangle');
wp1.geom.feature('substr').set('size',{num2str...
((total_width+sub_border*2)*1e-6),num2str...
((total_length+sub_border*2)*1e-6)});
wp1.geom.feature('substr').set('pos',{num2str...
(-sub_border*1e-6),num2str(-sub_border*1e-6)});



i = 0:1:length(yw);
rw_list=strread(sprintf('rw%d\n',i(:)),'%s')';
j = 0:1:length(yl);
rl_list=strread(sprintf('rl%d\n',j(:)),'%s')';
k = 1:1:length(x_bars);
vbar_list=strread(sprintf('vbar%d\n',k(:)),'%s')';
l = 1:1:length(y_bars);
hbar_list=strread(sprintf('hbar%d\n',l(:)),'%s')';

co1 = wp1.geom.feature.create('co1','Compose');
co1.set('intbnd','off');
co1.selection('input').set([rw_list rl_list 'Box']);
co1.set('formula',['Box' sprintf('-%s',rw_list{:},rl_list{:})]);
```

```
co2 = wp1.geom.feature.create('co2','Compose');
co2.set('intbnd','off');
co2.selection('input').set([hbar_list vbar_list 'co1']);
co2.set('formula',['co1' sprintf('+%s',vbar_list{:},hbar_list{:})]);

if same_side
   wp1.geom.create('C1','Square');
   wp1.geom.feature('C1').set('size',num2str(contact_size*1e-6));
   wp1.geom.feature('C1').set('pos',{num2str...
   (((total_width-contact_spacing)/2-...
   contact_size)*1e-6),num2str((-contact_distance-contact_size)*1e-6)});
   wp1.geom.create('C2','Square');
   wp1.geom.feature('C2').set('size',num2str(contact_size*1e-6));
   wp1.geom.feature('C2').set('pos',{num2str...
   (((total_width+contact_spacing)/2)*1e-6),num2str...
   ((-contact_distance-contact_size)*1e-6)});

   wp1.geom.create('cl1_1','Rectangle');
   wp1.geom.feature('cl1_1').set('size',{num2str...
   (contact_line_width*1e-6),num2str((contact_line_width*2)*1e-6)});
   wp1.geom.feature('cl1_1').set('pos',{num2str...
   (((total_width-contact_spacing-contact_size...
   -contact_line_width)/2)*1e-6),num2str((-contact_distance)*1e-6)});
   wp1.geom.create('cl1_2','Rectangle');
   wp1.geom.feature('cl1_2').set('size',{num2str...
   (contact_line_width*1e-6),num2str((contact_line_width*2)*1e-6)});
   wp1.geom.feature('cl1_2').set('pos',{num2str...
   (((total_width+contact_spacing+contact_size-...
   contact_line_width)/2)*1e-6),num2str((-contact_distance)*1e-6)});

   wp1.geom.create('cl2_1','Rectangle');
   wp1.geom.feature('cl2_1').set('base','center');
   wp1.geom.feature('cl2_1').set('size',{num2str...
   (abs((total_width-contact_spacing-contact_size-...
   bar_width(1))/2-x_bars(1))*1e-6),num2str(contact_line_width*1e-6)});
   wp1.geom.feature('cl2_1').set('pos',{num2str...
   (((total_width-contact_spacing-contact_size)/2-...
   ((total_width-contact_spacing-contact_size-...
   bar_width(1))/2-x_bars(1))/2)*1e-6),num2str...
   ((-contact_distance+contact_line_width*1.5)*1e-6)});
   wp1.geom.create('cl2_2','Rectangle');
   wp1.geom.feature('cl2_2').set('base','center');
   wp1.geom.feature('cl2_2').set('size',{num2str...
   (abs((total_width+contact_spacing+contact_size-bar_width...
   (end))/2-x_bars(end))*1e-6),num2str(contact_line_width*1e-6)});
   wp1.geom.feature('cl2_2').set('pos',{num2str...
   ((((total_width+contact_spacing+contact_size)/2)...
```

```
  -((total_width+contact_spacing+contact_size-bar_width...
  (end))/2-x_bars(end))/2)*1e-6),num2str((-contact_distance+...
  contact_line_width*1.5)*1e-6)});

  wp1.geom.create('cl3_1','Rectangle');
  wp1.geom.feature('cl3_1').set('size',{num2str(bar_width...
  (1)*1e-6),num2str((contact_distance-contact_line_width)*1e-6)});
  wp1.geom.feature('cl3_1').set('pos',{num2str(x_bars..
  (1)*1e-6),num2str(-(contact_distance-contact_line_width)*1e-6)});
  wp1.geom.create('cl3_2','Rectangle');
  wp1.geom.feature('cl3_2').set('size',{num2str...
  (bar_width(end)*1e-6),num2str((contact_distance...
  -contact_line_width)*1e-6)});
  wp1.geom.feature('cl3_2').set('pos',{num2str...
  (x_bars(end)*1e-6),num2str(-(contact_distance...
  -contact_line_width)*1e-6)});

  co3 = wp1.geom.feature.create('co3','Compose');
  co3.set('intbnd','off');
  co3.selection('input').set({'cl1_1' 'cl1_2' 'cl2_1' 'cl2_2' 'cl3_1'
     'cl3_2' 'co2'});
  co3.set('formula',['co2+cl1_1+cl1_2+cl2_1+cl2_2+cl3_1+cl3_2']);
else
   wp1.geom.create('C1','Square');
   wp1.geom.feature('C1').set('size',num2str(contact_size*1e-6));
   wp1.geom.feature('C1').set('pos',{num2str...
   ((-contact_distance-contact_size)*1e-6),...
   num2str((-contact_size+contact_line_width)/2*1e-6)});
   wp1.geom.create('C2','Square');
   wp1.geom.feature('C2').set('size',num2str(contact_size*1e-6));
   wp1.geom.feature('C2').set('pos',{num2str...
   ((total_width+contact_distance)*1e-6),num2str...
   ((-contact_size+contact_line_width)/2*1e-6)});

   wp1.geom.create('cl1_1','Rectangle');
   wp1.geom.feature('cl1_1').set('size',{num2str...
   ((contact_distance+x_bars(1))*1e-6),num2str...
   (contact_line_width*1e-6)});
   wp1.geom.feature('cl1_1').set('pos',{num2str...
   ((-contact_distance)*1e-6),'0'});
   wp1.geom.create('cl1_2','Rectangle');
   wp1.geom.feature('cl1_2').set('size',{num2str...
   ((total_width-x_bars(end)-bar_width(end)+...
   contact_distance)*1e-6),num2str(contact_line_width*1e-6)});
   wp1.geom.feature('cl1_2').set('pos',{num2str...
   ((x_bars(end)+bar_width(end))*1e-6),'0'});
```

```
    co3 = wp1.geom.feature.create('co3','Compose');
    co3.set('intbnd','off');
    co3.selection('input').set({'cl1_1' 'cl1_2' 'co2'});
    co3.set('formula',['co2+cl1_1+cl1_2']);
end


e1 = g1.feature.create('e1','Extrude');
e1.selection('input').set({'wp1.substr'});
e1.set('distance',num2str(-sub_thickness*1e-6));

g1.run;

% the following script introduces physics into the model

if same_side
    coords1=[((total_width/2-contact_spacing-contact_size)*1e-6)
        (total_width/2*1e-6); ((-contact_distance-contact_size/2)*1e-6)
        ((-contact_distance-contact_size*1.5)*1e-6); -5e-6 5e-6];
    term = mphselectbox(model,'geom1',coords1,'edge');
    coords2= [(total_width/2*1e-6)
        ((total_width/2+contact_spacing+contact_size)*1e-6);
        ((-contact_distance-contact_size/2)*1e-6)
        ((-contact_distance-contact_size*1.5)*1e-6); -5e-6 5e-6];
    gnd = mphselectbox(model,'geom1',coords2,'edge');
else
    coords1=[(-contact_distance-contact_size/2)*1e-6
        (-contact_distance-contact_size*1.5)*1e-6; -contact_size*1e-6
        contact_size*1e-6; -5e-6 5e-6];
    term = mphselectbox(model,'geom1',coords1,'edge');
    coords2=[(total_width+contact_distance+contact_size/2)*1e-6
        (total_width+contact_distance+contact_size*1.5)*1e-6;
        -contact_size*1e-6 contact_size*1e-6; -5e-6 5e-6];
    gnd = mphselectbox(model,'geom1',coords2,'edge');
end

mat1 = model.material('mat1');
mat1.selection.set([6 7 8]);
mat2 = model.material('mat2');
mat2.selection.set([1]);

ht = model.physics('ht');
temp1 = ht.feature('temp1');
temp1.selection.set([3]);
hf1 = ht.feature('hf1');
hf1.selection.set([4 6 7 8]);
tl1 = ht.feature('tl1');
```

```
tl1.selection.set([6 7 8]);

ecs = model.physics('ecs');
ecs.selection.set([6 7 8]);
gnd1 = ecs.feature('gnd1');
gnd1.selection.set(gnd);
term1 = ecs.feature('term1');
term1.selection.set(term);

bemh1 = model.multiphysics('bemh1');
bemh1.selection.set([6 7 8]);



model.param.set('tot_wid', num2str(total_width*1e-6))
model.param.set('tot_len', num2str(total_length*1e-6))

op_t_volt = 1:1:20;
op_t_thick = 0.25:0.25:2;

if volt_scan == 1

    model.param.set('Cr_t', '1e-6');
    for ap_vol = 1:1:20
        model.param.set('ap_vol', num2str(ap_vol*0.5));
        model.study('std1').run;

        hor_data=mphplot(model,'pg1');
        line_1=getfield(hor_data{1}{1},'d');
        line_2=getfield(hor_data{2}{1},'d');
        line_3=getfield(hor_data{3}{1},'d');
        peaks_1=findpeaks(-double(line_1));
        peaks_2=findpeaks(-double(line_2));
        peaks_3=findpeaks(-double(line_3));
        ave_1 = mean(-peaks_1(2:end-2));
        ave_2 = mean(-peaks_2(2:end-2));
        ave_3 = mean(-peaks_3(2:end-2));
        op_t_volt(ap_vol) = min([ave_1 ave_2 ave_3]);
    end
    model.param.set('Cr_t', num2str(cr_thickness*1e-6));
    [temp pos] = min(abs(op_t_volt./100-1));
    applied_voltage = pos*0.5;
    model.param.set('ap_vol', num2str(applied_voltage));
    model.study('std1').run;

else
```

```
    model.param.set('Cr_t', num2str(cr_thickness*1e-6));
    model.param.set('ap_vol', num2str(applied_voltage));
    model.study('std1').run;

end

mphsave(model,'ver1_5');
```

Bibliography

[1] FJ Morin. “Oxides which show a metal-to-insulator transition at the Neel temperature”. In: *Physical Review Letters* 3.1 (1959), p. 34.

[2] PJ Hood and JF DeNatale. “Millimeter-wave dielectric properties of epitaxial vanadium dioxide thin films”. In: *Journal of applied physics* 70.1 (1991), pp. 376–381.

[3] Andrea Cavalleri, Cs Tóth, Craig W Siders, et al. “Femtosecond structural dynamics in VO 2 during an ultrafast solid-solid phase transition”. In: *Physical Review Letters* 87.23 (2001), p. 237401.

[4] M Nakano, K Shibuya, D Okuyama, et al. “Collective bulk carrier delocalization driven by electrostatic surface charge accumulation”. In: *Nature* 487.7408 (2012), pp. 459–462.

[5] J Cao, E Ertekin, V Srinivasan, et al. “Strain engineering and one-dimensional organization of metal–insulator domains in single-crystal vanadium dioxide beams”. In: *Nature nanotechnology* 4.11 (2009), pp. 732–737.

[6] Jonathan Leroy, Aurelian Crunteanu, Annie Bessaudou, et al. “High-speed metal-insulator transition in vanadium dioxide films induced by an electrical pulsed voltage over nano-gap electrodes”. In: *Applied Physics Letters* 100.21 (2012), p. 213507.

[7] G Stefanovich, A Pergament, and D Stefanovich. “Electrical switching and Mott transition in VO2”. In: *Journal of Physics: Condensed Matter* 12.41 (2000), p. 8837.

[8] John B Goodenough. “The two components of the crystallographic transition in VO 2”. In: *Journal of Solid State Chemistry* 3.4 (1971), pp. 490–500.

[9] A Zylbersztejn and NF Mott. “Metal-insulator transition in vanadium dioxide”. In: *Physical Review B* 11.11 (1975), p. 4383.

[10] Shik Shin, S Suga, M Taniguchi, et al. “Vacuum-ultraviolet reflectance and photoemission study of the metal-insulator phase transitions in VO 2, V 6 O 13, and V 2 O 3”. In: *Physical Review B* 41.8 (1990), p. 4993.

[11] D Paquet and P Leroux-Hugon. “Electron correlations and electron-lattice interactions in the metal-insulator, ferroelastic transition in V O 2: A thermodynamical study”. In: *Physical Review B* 22.11 (1980), p. 5284.

[12] HK Kim, H You, RP Chiarello, et al. "Finite-size effect on the first-order metal-insulator transition in VO 2 films grown by metal-organic chemical-vapor deposition". In: *Physical Review B* 47.19 (1993), p. 12900.

[13] Michael EA Warwick and Russell Binions. "Thermochromic vanadium dioxide thin films from electric field assisted aerosol assisted chemical vapour deposition". In: *Solar Energy Materials and Solar Cells* (2015).

[14] LA Ryabova, IA Serbinov, and AS Darevsky. "Preparation and properties of pyrolysis of vanadium oxide films". In: *Journal of the Electrochemical Society* 119.4 (1972), pp. 427–429.

[15] F Cardillo Case. "Modifications in the phase transition properties of predeposited VO2 films". In: *Journal of Vacuum Science & Technology A* 2.4 (1984), pp. 1509–1512.

[16] F Co Case. "Influence of ion beam parameters on the electrical and optical properties of ion-assisted reactively evaporated vanadium dioxide thin films". In: *Journal of Vacuum Science & Technology A* 5.4 (1987), pp. 1762–1766.

[17] FC Case. "The influence of substrate temperature on the optical properties of ion-assisted reactively evaporated vanadium oxide thin films". In: *Journal of Vacuum Science & Technology A* 6.3 (1988), pp. 2010–2014.

[18] Francine C Case. "Effects of low-energy low-flux ion bombardment on the properties of VO2 thin films". In: *Journal of Vacuum Science & Technology A* 7.3 (1989), pp. 1194–1198.

[19] Francine C Case. "Low temperature deposition of VO2 thin films". In: *Journal of Vacuum Science & Technology A* 8.3 (1990), pp. 1395–1398.

[20] Francine C Case. "Improved VO 2 thin films for infrared switching". In: *Applied optics* 30.28 (1991), pp. 4119–4123.

[21] Mark Borek, F Qian, V Nagabushnam, et al. "Pulsed laser deposition of oriented VO2 thin films on R-cut sapphire substrates". In: *Applied physics letters* 63.24 (1993), pp. 3288–3290.

[22] DH Kim and HS Kwok. "Pulsed laser deposition of VO2 thin films". In: *Applied physics letters* 65.25 (1994), pp. 3188–3190.

[23] Ping Jin and Sakae Tanemura. "Formation and thermochromism of VO2 films deposited by RF magnetron sputtering at low substrate temperature". In: *Japanese journal of applied physics* 33.3R (1994), p. 1478.

[24] Yuzo Shigesato, Mikiko Enomoto, and Hidehumi Odaka. "Thermochromic VO2 films deposited by RF magnetron sputtering using V2O3 or V2O5 targets". In: *Japanese Journal of Applied Physics* 39.10R (2000), p. 6016.

[25] EE Chain. "The influence of deposition temperature on the structure and optical properties of vanadium oxide films". In: *Journal of Vacuum Science & Technology A* 4.3 (1986), pp. 432–435.

[26] KD Rogers, JA Coath, and MC Lovell. "Characterization of epitaxially grown films of vanadium oxides". In: *Journal of applied physics* 70.3 (1991), pp. 1412–1415.

[27] J Duchene, M Terraillon, and M Pailly. "RF and DC reactive sputtering for crystalline and amorphous VO 2 thin film deposition". In: *Thin Solid Films* 12.2 (1972), pp. 231–234.

[28] Songwei Lu, Lisong Hou, and Fuxi Gan. "Preparation and optical properties of phase-change VO2 thin films". In: *Journal of materials science* 28.8 (1993), pp. 2169–2177.

[29] Litao Kang, Yanfeng Gao, Zongtao Zhang, et al. "Effects of annealing parameters on optical properties of thermochromic VO2 films prepared in aqueous solution". In: *The Journal of Physical Chemistry C* 114.4 (2010), pp. 1901–1911.

[30] SM Babulanam, TS Eriksson, GA Niklasson, et al. "Thermochromic VO2 films for energy-efficient windows". In: *30th Annual Technical Symposium*. International Society for Optics and Photonics. 1987, pp. 8–18.

[31] Byung Gyu Chae, Hyun Tak Kim, and Sun Jin Yun. "Characteristics of W-and Ti-doped VO2 thin films prepared by sol-gel method". In: *Electrochemical and Solid-State Letters* 11.6 (2008), pp. D53–D55.

[32] GV Jorgenson and JC Lee. "Doped vanadium oxide for optical switching films". In: *Solar Energy Materials* 14.3 (1986), pp. 205–214.

[33] Nuru Mlyuka, Gunnar Niklasson, and Claes-Göran Granqvist. "Mg doping of thermochromic VO2 films enhances the optical transmittance and decreases the metal-insulator transition temperature". In: *Applied physics letters* 95.17 (2009), p. 171909.

[34] F Beteille and J Livage. "Optical switching in VO2 thin films". In: *Journal of Sol-Gel Science and Technology* 13.1-3 (1998), pp. 915–921.

[35] Ikuya Takahashi, Mitsuhiro Hibino, and Tetsuichi Kudo. "Thermochromic properties of double-doped VO2 thin films prepared by a wet coating method using polyvanadate-based sols containing W and Mo or W and Ti". In: *Japanese Journal of Applied Physics* 40.3R (2001), p. 1391.

[36] JM Reyes, M Sayer, and R Chen. "Transport properties of tungsten-doped VO2". In: *Canadian Journal of Physics* 54.4 (1976), pp. 408–412.

[37] KuanChang Pan, Weisong Wang, Eunsung Shin, et al. "Vanadium Oxide Thin-Film Variable Resistor-Based RF Switches". In: *Electron Devices, IEEE Transactions on* 62.9 (2015), pp. 2959–2965.

[38] Aurelian Crunteanu, Julien Givernaud, Jonathan Leroy, et al. "Voltage-and current-activated metal–insulator transition in VO2-based electrical switches: a lifetime operation analysis". In: *Science and Technology of Advanced Materials* 11.6 (2010), p. 065002.

[39] Arash Joushaghani, Brett A Kruger, Suzanne Paradis, et al. "Sub-volt broadband hybrid plasmonic-vanadium dioxide switches". In: *Applied Physics Letters* 102.6 (2013), p. 061101.

[40] Hong Ye, Xianchun Meng, and Bin Xu. "Theoretical discussions of perfect window, ideal near infrared solar spectrum regulating window and current thermochromic window". In: *Energy and Buildings* 49 (2012), pp. 164–172.

[41] Kazuhiro Kato, Pung Keun Song, Hidehumi Odaka, et al. "Study on thermochromic VO2 films grown on ZnO-coated glass substrates for "smart windows"". In: *Japanese journal of applied physics* 42.10R (2003), p. 6523.

[42] Gabriel M Rebeiz, Kamran Entesari, Isak C Reines, et al. "Tuning in to RF MEMS". In: *Microwave Magazine, IEEE* 10.6 (2009), pp. 55–72.

[43] Susmita Sinha, Sunipa Roy, and CK Sarkar. "Design and electro-thermal analysis of microheater for low temperature MEMS based gas sensor". In: *Proc. Int. Symp. Devices MEMS, Intelligent Systems and Communication (ISDMISC)*. 2011, pp. 26–31.

[44] KL Zhang, SK Chou, and SS Ang. "Fabrication, modeling and testing of a thin film Au/Ti microheater". In: *International Journal of Thermal Sciences* 46.6 (2007), pp. 580–588.